Edinburgh Research Explorer

Ruthenium-based catalysts supported on carbon xerogels for hydrogen production via ammonia decomposition

Ruthenium-based catalysts supported on carbon xerogels for hydrogen production via ammonia decomposition

S. Mazzone[1], T. Goklany[1], Guangru Zhang[2], Jinkun Tan[2], Evangelos I. Papaioannou[3], F.R. García-García[1]*

[1]*The University of Edinburgh, School of Engineering, Institute for Materials and Processes, Sanderson Building, The King's Buildings, Mayfield Road, EH9 3JL Edinburgh, Scotland, UK*

[2] *State Key Laboratory of Materials-Oriented Chemical Engineering, College of Chemical Engineering, Nanjing Tech University, 30 Puzhu Road(S), Nanjing 211816, P.R. China*

[3] *School of Engineering, Newcastle University, Newcastle-upon-Tyne, NE1 7RU, UK*

*Corresponding author: Francisco.Garcia-Garcia@ed.ac.uk, +44(0)131 6504860

Abstract

Carbon xerogels were synthesised and used as support of ruthenium-based catalysts for the ammonia decomposition reaction. To improve their physical-chemical properties, carbon xerogels were either activated in carbon dioxide atmosphere (for 1 and 5 hours), or doped with nitrogen via co-precursor method, using urea as nitrogen source. Un-promoted and sodium-promoted ruthenium catalysts were prepared by incipient wetness impregnation. All catalysts were tested during the ammonia decomposition reaction (1 atm, 100-600°C), showing high catalytic activity. The 5 hours carbon dioxide activation treatment resulted in a decrease in oxygen surface groups (*i.e.* by 11 wt. %) on carbon xerogels surface, and in an increase in the structure crystallinity (*i.e.* by 15% in the T_{Burn}) of carbon xerogels, resulting in a higher ammonia decomposition reaction rate (*i.e.* 3.5-fold at 450°C). Similarly, nitrogen addition to carbon xerogels had a positive effect on the catalysts basicity, enhancing their catalytic performance (*i.e.* triple reaction rate at 450°C). The addition of sodium conferred an enhancement in the performance of each catalyst (*i.e.* reaction rate up to 9 times higher at 450°C). Two ammonia decomposition reaction runs were performed for all catalysts, to test the performance reproducibility of the catalysts. It was found that un-promoted catalysts exhibited higher reaction rates (*i.e.* up to 3.5 times at 450°C) during the second run of reaction due to the larger ruthenium particle size, whereas sodium-promoted catalysts exhibited similar catalytic activity in both reaction runs due to the presence of sodium oxide avoiding the sintering of ruthenium particles.

1 Introduction

Ruthenium-based catalysts supported on CNTs have been suggested to be the most efficient catalysts for the ammonia decomposition reaction [1–4]. However, the high cost/performance ratio of CNTs have delayed the full breakthrough of this material in real life applications [5,6]. A promising alternative to CNTs are carbon xerogels, which have a wide range of textural and structural properties. Tailoring of these properties can be achieved by using different synthesis methods and post-synthesis treatments [7–10].

Previous studies demonstrated that the performance of the catalysts during the ammonia decomposition reaction is support-dependent [1,2,11,12]. For instance, it has been reported that the activity of CoMo nitrides in ammonia decomposition increases with the surface acidity and the surface area of the supports [12]. Likewise, nickel-based catalysts were found to be inactive when supported on carbon materials, and highly active during the ammonia decomposition when supported on ceramic materials [2]. On the contrary, it has been reported that the ideal support of catalysts based on iron, cobalt and ruthenium for the decomposition of ammonia should feature several properties, such as i) thermal stability under the reaction conditions, ii) large specific surface area, iii) electron conductivity, iv) low concentration of electron-withdrawing functional groups, and v) high basicity [2,4,13–15]. In accordance with these properties, carbonaceous materials, including active carbons (ACs), high surface area graphite (HSAG), CNTs and carbon nanofibers (CNFs) have been considered as the most suitable support for ruthenium-based catalysts for the ammonia decomposition reaction [3,4,16–19].

Raróg et al. proposed the use of ACs as catalyst support for the ammonia decomposition reaction due to their high surface area, responsible for an enhanced metal dispersion, which increases the catalytic activity during the reaction [16]. To improve the electronic conductivity of ACs, thermal treatment at high temperature in an inert atmosphere have been used [14,15]. Particularly, the thermal treatment resulted in ACs with higher graphitisation degree and less electron-withdrawing groups on the surface, which are requirements for the ammonia decomposition reaction [14]. Despite the AC-supported catalysts were found to be highly active for this reaction, their difficult reproducibility make difficult their use as catalyst support [20].

2

As alternative to AC, Sørensen et al. proposed HSAG as catalyst support for the ammonia decomposition reaction [19]. In addition to the high surface area, HSAG offer high conductivity and high thermal stability under reaction conditions, which is beneficial for the inhibition of methanation and the suitability of HSAG as a catalyst support in wider temperature range applications. In this respect, Rossetti et al. [21] indicated that the methanation rate of the carbon support is reduced by increasing its graphitisation degree.

Despite the larger specific surface area of other carbon materials previously used, Yin et al. proposed CNTs as optimal catalyst support for the ammonia decomposition reaction, due to their excellent conductivity [1–4]. Even though the ruthenium metal particles dispersion on AC and CNTs was found to be very similar, the CNTs-supported catalyst gave rise to an ammonia decomposition reaction rate three times higher than that of the AC-supported catalyst. This was mainly attributed to the higher electron transfer between CNTs and the metal, which promote the nitrogen desorption, known as the reaction limiting step [22]. However, CNTs present several drawbacks, including high cost, difficulty to synthesise on large scale, presence of acidic surface functionalities, and methanation at low temperature (*i.e.* 423°C), which have always limited their use industrial applications [5,6].

Based on their physical-chemical properties, Duan et al. proposed CNFs as promising alternative catalyst support to CNTs for the ammonia decomposition reaction [18]. Indeed, their study revealed that CNFs-supported ruthenium catalysts were highly active for hydrogen production via ammonia decomposition. Moreover, despite the lower graphitisation degree of CNFs compared to CNTs, the former lead to higher catalytic activities. This was attributed to peculiar surface properties of CNFs, which enhanced the metal dispersion and the electronic properties of the catalyst, as well as their higher stability [23]. Even though CNFs could be considered as highly effective catalyst support for the ammonia decomposition, similarly to CNTs, their use in industrial-scale applications is hindered by their poor reproducibility and their high cost [20].

It is well known that high electron transfer from electropositive elements to the active metal surface is needed to promote the ammonia decomposition reaction rate-limiting step, *i.e.* the recombinative nitrogen desorption [11]. In this respect, the use of alkali promoters, such as cesium, sodium and potassium, has been widely proposed in order to further improve the performance of catalysts based on iron, cobalt or ruthenium during the ammonia decomposition [11,15,16,24–26]. More recently, in order to

enhance the physical and chemical properties of conventional carbon materials (*i.e.* basicity and electrical conductivity), and maximise the ammonia conversion at lower temperatures, their nitrogen functionalisation has been studied [9,17,27]. Stöhr et al. showed that nitrogen doping resulted in carbon materials with higher thermal stability and resistance to oxidation [27]. Moreover, the incorporation of nitrogen atoms in the carbon lattice has been found to enhance surface basicity and graphitisation degree of carbon materials [28–31]. In this respect, García-García et al. showed that ruthenium catalysts supported on N-doped CNTs were more active than their non-doped counterparts [17]. This can be explained due to the electron donor effect of nitrogen atoms, which modify the electronic structure of the catalyst support enhancing its interaction with metal particles [17,32].

Over the last years, carbon xerogels have gained considerable interest in the catalysis research field due to their structure and surface versatility [9,33–37]. Carbon xerogels are obtained from the carbonisation of organic xerogels, which are synthesised by the conventional sol-gel method originally proposed by Pekala, using resorcinol and formaldehyde as organic starting monomers [38]. Maldonado-Hódar et al. firstly proposed the use of carbon xerogels as catalyst support, due to the fact that they show large specific surface area, excellent electrical conductivity and high purity [39]. These properties can be adapted according to the requirements of a specific application, which is indicative of a considerable advantage of carbon xerogels being a porous carbon material [39]. Despite the interest in utilising carbon xerogels as catalysts support for a wide range of reactions, including oxidation [34], hydrogenation [35,40,41], and ozonation [37], their use in the ammonia decomposition reaction has never been reported. The hierarchical pore structure of carbon xerogels permits the fine-tuning of micro- and mesoporosity during synthesis and carbonisation processes, as well as by means of physical or chemical activation treatments [7,8,42], allowing to control their surface area, surface chemistry and conductivity. Additionally, several synthesis or post-synthesis methods can be employed to induce surface basicity via functionalisation and nitrogen doping, in order to improve their suitability as a catalyst support for the ammonia decomposition reaction [9,10,36,43,44].

The aim of this work is to synthesise, characterise and study the catalytic activity of a set of un-promoted and sodium-promoted ruthenium-based catalysts supported on carbon xerogels for hydrogen production via ammonia decomposition. Our hypothesis is that carbon xerogels can be established as efficient catalyst supports, and as a valid alternative to carbon materials previously used. In order to improve their suitability as

a catalyst support, carbon xerogels were either activated in carbon dioxide atmosphere or nitrogen doped via co-precursor method, using urea as nitrogen source. Furthermore, the effect of i) textural and structural properties of carbon xerogels, ii) ruthenium particle size distribution, iii) addition of sodium as promoter, on the catalytic performance and thermal stability of the catalyst during the reaction were investigated.

2 Experimental section

2.1 Synthesis of carbon xerogels

Resorcinol-formaldehyde xerogels were synthesised by the conventional sol-gel method, originally proposed by Pekala [38]. A starting solution of resorcinol, formaldehyde and water, containing 30 wt. % solids was prepared, where the molar ratios of resorcinol to carbonate (R/C) and resorcinol to formaldehyde (R/F) were fixed at 200 and 0.5, respectively. The solution was stirred for 30 min, followed by 3 days of gelation and curing in a ventilation oven (SciQuip Oven 55S) at 85°C. The obtained gel was dried for 3 days at in a ventilation oven (SciQuip Oven 55S) 100°C.

The carbon xerogel, labelled as CX, was obtained by pyrolysis of the dried xerogel at 800°C in nitrogen atmosphere (*i.e.* 100 $cm^3 \cdot min^{-1}$ (STP)) using a tubular furnace (MTI Corporation, OTF-1200X). Activated carbon xerogels, labelled as ACX_{1h} and ACX_{5h}, were obtained by treating the CX in carbon dioxide atmosphere (*i.e.* 25 $cm^3 \cdot min^{-1}$ (STP)) at 800°C for 1h and 5 h, respectively.

The nitrogen-containing dried xerogel was synthesised via co-precursor method using urea as nitrogen source. The R/F, R/C and Resorcinol/Urea (*i.e.* R/U) ratios were fixed at 200, 0.5, and 2, respectively. Like in the previous synthesis, the solution was stirred for 30 min, followed by 3 days of gelation and curing in a ventilation oven (SciQuip Oven 55S) at 85°C. The obtained gel was dried for 3 days at in a ventilation oven (SciQuip Oven 55S) 100°C. The nitrogen-doped carbon xerogel, labelled as UCX, was obtained by pyrolysis of the nitrogen-containing dried xerogel at 800°C in nitrogen atmosphere (*i.e.* 100 $cm^3 \cdot min^{-1}$ (STP)) using a tubular furnace (MTI Corporation, OTF-1200X) [9].

A schematic diagram of the thermal treatments used to synthesise all of the different carbon xerogels employed in this study is shown in Figure 1.

5

2.2 Characterisation of carbon xerogels

2.2.1 Nitrogen adsorption/desorption isotherms

The surface area and pore volume of each support were determined studying nitrogen adsorption/desorption isotherms. The sample was firstly degassed at 150°C for 150 min, then nitrogen adsorption/desorption measurements were taken at -196°C (iQ autosorb, Quantachrome). The BET and BJH methods were applied to calculate the specific surface area and the pore size distribution of the sample, respectively.

2.2.2 Temperature Programmed Desorption

Temperature programmed desorption (TPD) analysis was carried out to identify oxygen functional groups exposed on the surface of the carbon xerogels. The sample was loaded into a U-shape quartz glass cell, connected to the analyser (iQ autosorb, Quantachrome), ensuring that there were no leaks, in order to guarantee under vacuum conditions. The analyser was connected in-line to a mass spectrometer (HAL-201, HIDEN ANALYTICAL). The experiment was performed from room temperature to 700°C, under a 50 $cm^3 \cdot min^{-1}$ (STP) flow of pure helium.

2.2.3 Thermal Gravimetric analysis in nitrogen atmosphere

Oxygen surface groups were quantified by thermal gravimetric analysis under nitrogen flow (N_2-TGA), using a METTLER TOLEDO thermogravimetric analyser (TGA/DSC 3+). The sample was heated up to 700°C using a 10°Cmin^{-1} temperature ramp. A nitrogen flowrate of 20 $cm^3 \cdot min^{-1}$ (STP) was flowed throughout the experiment. The weight loss, in specific temperature ranges, will correspond to the amount in weight of the several oxygen surface groups identified via TPD analysis.

2.2.4 Thermal Gravimetric analysis in air atmosphere

The thermal stability of the different carbon xerogels was evaluated by determining their burning temperatures via thermal gravimetric analysis in air atmosphere (Air-TGA). The sample was heated up to 800°C, under a 20 $cm^3 \cdot min^{-1}$ (STP) flow of air, using the same apparatus used for N_2-TGA experiments.

2.2.5 Scanning Electron Microscopy

The morphology of the supports was determined using a Jeol, Jsm-it100 scanning electron microscope (SEM), operated at 20kV. The samples were uncoated.

2.3 Synthesis of ruthenium-based catalysts supported on carbon xerogels

Carbon xerogels here synthesised were used as supports of ruthenium-based catalysts. Un-promoted catalysts were prepared by incipient wetness impregnation method, starting from a solution of $Ru(NO)(NO_3)_3$ to get 1.5 wt.% of ruthenium. After impregnation, catalysts were dried overnight at 110°C.

The resulting catalysts were labelled as Ru-CX, Ru-ACX$_{1h}$, Ru-ACX$_{5h}$, and Ru-UCX, according to the impregnated supports.

In order to get sodium-promoted catalysts, a sequential impregnation was carried out, using a water solution of NaOH to get 5 wt.% of sodium. After impregnation, catalysts were dried overnight at 110°C.

The resulting catalysts were labelled as Ru/Na-CX, Ru/Na-ACX$_{1h}$, Ru/Na-ACX$_{5h}$, and Ru/Na-UCX, according to the impregnated supports.

2.4 Characterisation ruthenium-based catalysts supported on carbon xerogels

2.4.1 Transmission Electron Microscopy

Metal particle size distribution was estimated by transmission electron microscopy (TEM) using a Jeol TEM-1400 Plus. The samples were dispersed by ultrasonic treatment in an ethanol solution, placed on the copper TEM grid coated with a carbon film, and finally the solvent was slowly evaporated. Since a large number of nanoparticles is needed for a high-quality particle size distribution, about 300 nanoparticles were analysed for each catalyst. Particles shown in the TEM images were analysed using the ImageJ software. The diameter of ruthenium metal particles, which are assumed spherical, was estimated using the Automated Counting function built-in the software, which has an accuracy of 98%.

Moreover, the metal particles dispersion over the catalysts support was estimated from the TEM metal particle size distributions using the Eq.1, assuming that the dominant crystal structure of ruthenium is hexagonal closed pack (hcp) with lattice parameters equal to $a= b= 0.27$ nm and $c= 0.43$ nm [45].

$$D\ (\%) = \frac{A_{tot}}{V_{tot}} \times \frac{v}{s} = \frac{\sum n_i d_i^2}{\sum n_i d_i^3} \times \frac{6a}{\sqrt{3}} \qquad \text{Eq.1}$$

Where A_{tot} is the total surface area, V_{tot} is the total volume, v is the atomic volume, s is the atomic surface area, n_i is the number of particles with diameter d_i.

Finally, to understand the composition and the distribution of ruthenium and sodium particles on the catalyst's support surface, as well as their mutual position, the sodium-promoted catalysts herein studied have been analysed via Scanning Transmission

Electron Microscopy under high-angle annular dark field mode (HAADF-STEM) and Energy Dispersive X-ray Spectroscopy (EDS). The experiments were carried out with a Titan Themis 200 microscope (FEI) equipped with an X-FEG Schottky field emission gun operated at 200 kV. Samples were prepared by dispersing the catalysts in ethanol; a drop of the suspension was then allowed to evaporate on a holey carbon coated copper grid.

2.4.2 Temperature Programmed Reduction

Temperature programmed reduction (TPR) analysis was carried out in an automated gas sorption analyser (autosorb iQ, Quantachrome). Each sample was loaded into a U-shape quartz glass cell, connected to the gas sorption analyser. All desorbing gases were detected using a mass spectrometer (HAL-201, HIDEN ANALYTICAL), connected to the analyser. The experiments were performed between 25°C and 700°C, with a temperature ramp of $10°C \cdot min^{-1}$, using a 25 $cm^3 \cdot min^{-1}$ (STP) flow of 5% vol hydrogen balanced in argon.

2.4.3 X-ray photoelectron spectroscopy

The surface chemical composition of each catalyst was analysed by X-ray photoelectron spectroscopy (XPS), using an X-ray photoelectron spectrometer (Thermo ESCALAB 250, USA) equipped with an Al-Kα X-ray source (1486.7 eV). The bond energies were referenced to the adventitious C 1s line (284.6 eV). The error in determination of electron binding energies and the line widths did not exceed 0.2 eV. The C1s, O1s, N1s, Ru3d and Na1s envelopes were curve-fitted using Gaussian component profiles using the Origin peak-fitting software. A Shirley baseline was used for sloping backgrounds.

2.5 Performance of ruthenium-based catalysts supported on carbon xerogels during the ammonia decomposition reaction

2.5.1 Experimental apparatus

The experimental apparatus used to study the performance of the ruthenium-based catalysts in the ammonia decomposition reaction consisted in: i) packed bed reactor (PBR), ii) reactor furnace (Elite Thermal Systems Limited. Model No: TSV12/32/150), iii) gas delivery system, iv) network of electrical line heaters, and v) mass spectrometer (EcoSys-PTM Mass Spectrometer).

The equipment was controlled via a computer programme written using LabVIEW systems engineering software, allowing open/close the valves of the gas delivery

system. The computer was also connected to the mass spectrometer to get real-time readings of the gas composition circulating in the system. Ammonia condensation within the lines was prevented by a network of electrical line heating tape and thermal insulating fabric, which kept the line temperatures above 150°C. The temperature of each of these lines was monitored using several k-type thermocouples distributed throughout the equipment.

2.5.2 Experimental procedure during the ammonia cracking reaction

In a typical reaction experiment 300 mg of catalyst (w_{cat}), were loaded in the packed bed reactor. Prior the reaction test, the catalyst was reduced in situ at 400°C under a 50 $cm^3 \cdot min^{-1}$ (STP) of 50% vol. hydrogen in argon. Then, the catalyst was exposed to 10% vol. ammonia balanced in argon, from 100°C to 600°C under atmospheric pressure. In all the experiments, the feed gas flow rate was set to be 100 $cm^3 \cdot min^{-1}$ (STP). The whole experiment has been designed in such a way that internal and external diffusion limitations have been minimised. In this respect, to obtain a Thiele modulus $\phi^2 \leq 0.4$, the samples were crushed and sieved to sizes ranging from 125 µm to 250 µm using stainless-steel sieves (Fieldmaster 78-800).

The composition of the exit gases was monitored by in-line the mass spectrometer, which was calibrated using pure argon as a zero gas, and the reaction mixture (10% vol. ammonia in argon) as a calibration gas. In addition, the ion current of both the pure argon and reaction mixture were used as references to calculate the range between 100% and 0% ammonia conversion, respectively. The ammonia conversion x_{NH_3} (%), was estimated using the following equation:

$$x_{NH_3} = \frac{C_{NH_{3_{in}}} - C_{NH_{3_{out}}}}{C_{NH_{3_{in}}}} \times 100$$
Eq.2

The error analysis of the experimental apparatus showed that the ammonia conversion absolute error is $\pm 1 \times 10^{-3}$, with mass spectrometer signals (ppb level).

The TOF of each catalyst herein studied was estimated assuming that the metallic phase is responsible for the catalyst activity. The following equation was used to calculate the TOFs:

$$TOF = \frac{\dot{n}_{NH_3}}{n_{Ru}} \times \frac{1}{D}$$
Eq.3

Where $\dot{n}_{NH_3}$ is the molar flowrate of the ammonia converted, n_{Ru} is the ruthenium loading in moles, which depends on both the metal and catalyst loadings (*i.e.* n_{Ru} = (catalyst loading x Ru loading)/Ru molecular weight), and D is the metal dispersion.

Furthermore, long-term (*i.e.* 100 h) stability tests at 450°C have been performed to study ammonia conversion levels over longer intervals of time. Finally, after the long-term stability test, the metal loading of both un-promoted and sodium-promoted catalysts were determined via Inductively Coupled Plasma Mass Spectrometry (ICP-MS). With this scope, samples were firstly leached in hot aqua regia (*i.e.* HCl/HNO$_3$ mix) for 48 h to dissolve the carbon substrate, and analysed using a Thermo Scientific X-Series2 ICP-MS.

3 Results

3.1 Characterization of carbon xerogels

3.1.1 Nitrogen adsorption/desorption isotherms

Nitrogen adsorption/desorption isotherms at -196°C and pore size distributions of carbon xerogels here studied are shown in Figure 2A and Figure 2B, respectively. According to the IUPAC classification, all isotherms are Type IV, which is typical for mesoporous materials [46]. Moreover, all samples presented an hysteresis loop which due to capillary condensation, typically observed in pores wider than 4 nm [46]. Hence, ACX$_{5h}$ shows a hysteresis loop Type H4 according to the IUPAC classification, common for micro-mesoporous carbon material with slit-shaped pores. However, the remaining supports show a hysteresis loop Type H2, which is indicative of a wide pore size distribution [46].

The duration of the carbon dioxide activation treatment had opposing effects on the surface area and total pore volume of ACX$_{1h}$ and ACX$_{5h}$. As can be seen in Figure 2, ACX$_{1h}$ shows higher surface area and total pore volume (*i.e.* 1384 m$^2 \cdot$g^{-1} and 0.407 cm$^3 \cdot$min^{-1}, respectively) than CX (*i.e.* 1050 m$^2 \cdot$g^{-1} and 0.389 cm$^3 \cdot$min^{-1}, respectively). On the contrary, ACX$_{5h}$ presents smaller surface area and total pore volume (*i.e.* 960 m$^2 \cdot$g^{-1} and 0.279 cm$^3 \cdot$min^{-1}, respectively) with respect to CX. Likewise, UCX exhibits lower surface area and total pore volume (*i.e.* 550 m$^2 \cdot$g^{-1} and 0.244 cm$^3 \cdot$min^{-1}, respectively) compared to CX. Surface area, total pore volume, and micro- and mesopore volume of all supports here studied are listed in Table 1.

Furthermore, Table 2 compares carbon xerogels here studied with those reported in the literature.

3.1.2 Temperature Programmed Desorption

Oxygen surface groups present on carbon xerogels surface were determined by Temperature Programmed Desorption (TPD) experiments. As it is well known oxygen surface groups decompose into carbon dioxide and carbon monoxide at medium and high temperatures [47]. The evolution of carbon dioxide and carbon monoxide desorption profiles with the temperature are shown in Figure 3A and Figure 3B, respectively. As can be seen in Figure 3A, carbon dioxide desorption profiles can be deconvoluted into three components, corresponding to carboxylic acids (*i.e.* peak a: 230 - 300°C), anhydrides (*i.e.* peak b: 400 - 450°C), and lactones (*i.e.* peak c: 530 - 580°C).

However, carbon monoxide desorption profiles, shown in Figure 3B, only exhibited one peak (*i.e.* peak d: 440 - 450°C) , which can be associated to the presence of anhydrides on the surface of carbon xerogels [47].

3.1.3 Thermal Gravimetric Analysis

The weight percentage of the different functional groups present on the surface of all supports here studied is reported in Table 3. Oxygen surface groups represent about the 14%, 9%, 3%, and 5% of the total mass of CX, ACX_{1h}, ACX_{5h}, and UCX, respectively, as determined by N_2-TGA.

As shown in **Error! Reference source not found.**A, among all the supports studied, CX shows the greatest drop in mass in air atmosphere, with a final mass loss of 63% at 700°C. On the contrary, UCX exhibits the smallest drop, with approximately 50% of its mass being lost after the treatment at 700°C.

The first derivative of each Air-TGA profile, indicating the temperature at which the rate of burning is maximised, is shown in **Error! Reference source not found.**B. Moreover, all burning temperatures are listed in Table 3.

CX, ACX_{1h}, ACX_{5h}, and UCX have inflection points of 550°C, 580°C, 600°C, and 640°C, respectively.

3.1.4 Scanning Electron Microscopy

Scanning Electron Microscopy (SEM) studied the morphology of the different supports. Different top surface SEM pictures from low to high magnification are depicted in Figure 4. It can be seen that UCX had the largest grain size, and that the grain size of non-doped supports increased after the activation treatment in carbon dioxide atmosphere.

3.2 Characterization of ruthenium-based catalysts supported on carbon xerogels

3.2.1 Transmission Electron Microscopy

Representative Transmission Electron Microscopy (TEM) images of un-promoted and sodium-promoted ruthenium-based catalysts here studied are displayed in Figure 5 and Figure 6, respectively. Notice that for both catalytic systems TEM images were taken before and after reaction. Fine ruthenium nanoparticles homogeneously dispersed on the support surface were observed in all catalysts.

Ruthenium particle size distribution histograms before and after the first reaction run, for un-promoted and sodium-promoted catalysts, are shown in Figure 5 and Figure 6, respectively. It can be seen that the centre of the ruthenium particle size distributions of un-promoted catalysts shifted towards bigger particle sizes after the first reaction run (*i.e.* black histogram), showing an higher concentration of particles between 2.4 and 2.8 nm. In contrast, the ruthenium particle size of all promoted catalysts remained constant after the first reaction run.

Furthermore, the standard deviation (SD) of ruthenium particle size distributions has been calculated for all catalysts herein presented. As can be seen from the data reported in Table 4, a similar SD trend can be identified for both un-promoted and sodium-promoted catalysts before reaction; in this respect, it can be noticed that the catalysts supported on ACX_{5h} and CX always present the narrowest and the widest particle size distribution, respectively. Likewise, only the two catalysts supported on ACX_{1h} presented a narrower particle size distributions after the first reaction experiment (*i.e.* SD 25% and 10% lower for Ru- ACX_{1h} and Ru/Na- ACX_{1h}, respectively).

Figure 7 shows conventional scanning transmission electron microscopy (STEM) high-angle annular dark-field (HAADF) images and corresponding Energy Dispersive X-ray Spectroscopy (EDS) elemental maps of the sodium-promoted catalysts herein studied. From a visual inspection of the elemental maps, it can be seen an even distribution of both ruthenium and sodium nanoparticles on the catalyst's support surface, indicating the absence of apparent ruthenium aggregates.

3.2.2 Temperature Programmed Reduction

Temperature Programmed Reduction (TPR) profiles of un-promoted and sodium-promoted catalysts are shown in Figure 8A and Figure 8B, respectively. The interpretation of these profiles has been done using the open literature [26,32,48,49]. For un-promoted catalysts, TPR profiles can be deconvoluted in three hydrogen consumption contributions at: i) low temperature (*i.e.* peak *a*: 210 - 245°C)

corresponding to the reduction of ruthenium oxide particles, ii) intermediate temperature (*i.e.* peak *b*: 335 - 420°C) corresponding to the hydrogen spillover, and iii) high temperature (*i.e.* peak *c*: 500 - 600°C) corresponding to the methanation of the support.

Likewise, TPR profiles of sodium-promoted catalysts, can be deconvoluted in two components at: i) low temperature (*i.e.* peak *d*: 375 - 390°C), and ii) high temperature (*i.e.* peak *e*: 540 - 615°C). Figure 8C shows a schematic diagram reporting the evolution of the catalyst surface of both un-promoted and sodium-promoted catalysts during the hydrogen TPR experiments.

3.2.3 X-ray photoelectron spectroscopy

Deconvolutions of X-ray photoelectron spectroscopy (XPS) spectra of C1s, O1s and N1s regions, for un-promoted and sodium-promoted ruthenium catalysts, prior to their activation, are reported in Figure 9A and Figure 9B, respectively.

About the C1s region, four contributions were identified in the XPS spectra of all catalysts: dehydrogenated carbon species bound to a metal ion (*i.e.* around 281 eV), amorphous carbon (*i.e.* 284.6–284.9 eV), carbon in lactone groups (*i.e.* 286.2–286.7 eV), and carbon in carboxylic groups (*i.e.* 288.6–288.8 eV). An additional contribution (*i.e.* around 283eV) was identified in the XPS spectra of the C1s region of all sodium-promoted catalysts, which can be attributed to the formation of carbon-sodium bonds [9,17,50,51]. Moreover, as a consequence of the nitrogen doping, both Ru-UCX and Ru/Na-UCX exhibited a further contribution in the C1s region, due to carbon-nitrogen bond [9,50,52].

Likewise, monitoring the Ru3d XPS region, which overlaps with the C1s one, an additional peak, ascribed to the presence of the ruthenium oxide (*i.e.* Ru(IV)) on the catalysts surface (*i.e.* about 280.7 eV) [53], is included in the deconvolution of the C1s XPS spectra of all catalysts herein studied.

As shown in Figure 9A and Figure 9B, the deconvoluted O1s region XPS spectra can be related to the following contributions [17,52]: ruthenium oxide (*i.e.* approx. 529 and 531 eV), oxygen in lactone groups (*i.e.* 532.7–533.0 eV) and oxygen in carboxylic groups (*i.e.* 533.8–534.4 eV). Moreover, an additional peak is included in the deconvolution of the O1s region of all sodium-promoted ruthenium catalysts (see Figure 9B), which suggests the presence of sodium oxide on the catalyst surface (*i.e.* about 530 eV) [54].

Similarly, for all N1s region XPS spectra, nitrogen components at high binding energy (*i.e.* around 402.4 and 406 eV) were identified, which can be attributed to NOx groups

generated by the thermal decomposition of the ruthenium precursor RuNO(NO$_3$)$_3$ used in the synthesis of the catalyst [55]. As expected, Ru-UCX and Ru/Na-UCX N1s region XPS spectra presented three additional nitrogen contributions, accounting for pyridinic nitrogen or N-6 (*i.e.* 399.5–398.5 eV), pyrrolic nitrogen or N-5 (*i.e.* 400.8–399.8 eV), and quaternary nitrogen or N-Q (*i.e.* 403.0–401.0 eV) [9,17,50,53].

3.3 Performance of ruthenium-based catalysts supported on carbon xerogels during the ammonia decomposition reaction

The reaction rates of both un-promoted and sodium-promoted ruthenium catalysts are shown in Figure 10 and Figure 11, respectively. Two reaction runs were carried out in order to evaluate the performance reproducibility of the catalysts during the ammonia decomposition reaction.

It can be seen that, all catalysts here studied presented a similar behaviour, being active from 350-400°C. Moreover, all un-promoted catalysts exhibited higher reaction rates during the second reaction run compared to the first reaction run.

As shown in Figure 11A, the addition of sodium had a positive effect on the performance of all the catalysts here studied, as reflected in their reaction rates. Furthermore, in contrast with the behaviour of the un-promoted catalysts, the catalytic behaviour of sodium-promoted catalysts did not change after the first reaction run.

Finally, as can be seen in Figure 10B and Figure 11B, all catalysts here studied showed constant ammonia conversions during the 100 h reaction experiment, proving their stability throughout the whole ammonia decomposition reaction under the operating conditions adopted (*i.e.* 450°C, 1 atm).

4 Discussion

4.1 Characterization of carbon xerogels

4.1.1 Nitrogen adsorption/desorption isotherms

From the data reported in Table 2, it can be noticed that CX showed higher surface area (*i.e.* 1050 m^2·g^{-1}) than carbon xerogels previously reported in the literature (*i.e.* 600-770 m^2·g^{-1}) [42,43,50,56–60]. This phenomena could be explained due to the low R/C ratio (*i.e.* R/C = 200) used in this work to synthesise the xerogel precursor. As stated by Pekala et al., the R/C ratio can significantly influence the kinetic of the gelation reaction and thus final properties of the xerogel [38,61]. In particular, low R/C ratios result in xerogels with small pore size and larger surface areas, whereas high R/C ratios lead to xerogels with bigger pores and lower surface areas [61].

14

Furthermore, Salinas-Torres et al. found that the R/C ratio has a strong influence on the pore texture of the dried xerogels and, therefore on their pyrolysed counterparts [62].

The effect of the carbon dioxide activation treatment on textural and structural properties of CX is shown in Figure 2. It can be seen that at low relative pressure (*i.e.* P/P_0 < 0.1 bar), ACX_{1h} adsorbed 20% more nitrogen than CX, indicating an increase of the microporosity after 1 h of carbon dioxide activation treatment. This development of the microporosity can be explained due to two factors; i) desorption of oxygen surface groups at the entrance of micropores, ii) opening of the micropores due to the reverse Boudouard reaction (*i.e.* $CO_2 + C \rightleftarrows 2\ CO$) [63].

On the other hand, as reported in Table 1, after 5 h of carbon dioxide activation treatment, the total pore volume of CX significantly decreased, as can be also deduced from the low volume of N_2 adsorbed by ACX_{5h}. This phenomenon could be explained due to the partial crystallisation of the support, which led to a more ordered structure. This result agrees with previous studies, pointing out that carbon xerogels with a more ordered carbonaceous structure present lower surface area and pore volume [64].

Among all carbon xerogels here studied, UCX presented the lowest surface area and pore volume, which suggests that this support presents a more ordered structure. As reported by Sousa et al. [36] and Rocha et al. [37], carbon xerogels obtained via co-precursor method using urea exhibit higher contributions of pyrrolic and quaternary nitrogen, which could explain the higher crystallinity observed in UCX. Likewise, UCX surface area (*i.e.* 550 m^2g^{-1}) is in line with those reported in the literature (*i.e.* 400-600 m^2g^{-1}) [9,36,43,44].

4.1.2 Temperature Programmed Desorption

Carbon dioxide and carbon monoxide TPD profiles of carbon xerogels are shown in Figure 3A and Figure 3B, respectively. The nature of oxygen surface groups identified in carbon xerogels here studied (*i.e.* carboxylic, anhydride and lactone) is in agreement with the results of previous works in which the synthesis of carbon xerogels were conducted under similar experimental conditions [36,37,42].

4.1.3 Thermal Gravimetric analysis in nitrogen atmosphere

As it is shown in Table 3, the amount of oxygen surface groups presented in CX decreased after the carbon dioxide activation treatment. Particularly, N_2-TGA experiments showed that ACX_{1h} and ACX_{5h} presented 5 wt. % and 11 wt. % less oxygen surface groups than CX, respectively. This behaviour can be justified by to the

exposure of CX to high temperature during the activation treatment (i.e. 800°C). Indeed, thermal treatments at high temperature (*i.e.* > 700°C) are widely used to remove functional groups from the carbon surface in order to enhance its physical and chemical properties (*i.e.* basicity and electrical conductivity) [14]. Despite the high temperature activation treatment, desorption of surface groups at low temperature was observed in both ACX_{1h} and ACX_{5h}, which can be explained due to the re-oxidation of the supports after the activation treatment when exposed to the atmosphere.

Likewise, the presence of nitrogen heteroatoms in the carbon xerogel caused a decrease in anhydride and lactone surface groups (*i.e.* 0.9 wt. % and 0.5 wt. %, respectively). This suggests that the formation of nitrogen surface groups during the pyrolysis of the nitrogen-doped carbon xerogel precursor could avoid the formation of certain oxygen surface groups such as lactone surface groups [65,66].

4.1.4 Thermal Gravimetric analysis in air atmosphere

Based on the data reported in Table 3, it can be seen that after the carbon dioxide activation treatment, the burning temperature of both ACX_{1h} and ACX_{5h} (*i.e.* 580°C and 600°C, respectively) was higher than that of CX (*i.e.* 535°C). The enhanced thermal stability observed for treated carbon xerogels can be explained due to an arrangement of carbon atoms into a more ordered crystal structure. This explanation is in line with the previous work of Zhong et al., which reported that the higher the crystallinity of carbon supports, the higher their thermal stability is [14].

Likewise, about UCX, the nitrogen doping led to an increase in the burning temperature (*i.e.* 640 °C), alluding to the presence of nitrogen atoms into the carbon lattice. As observed by Sousa et al. [36] and Rocha et al. [37], carbon xerogels synthesised via co-precursor method using urea result in carbon material with nitrogen atoms uniformly distributed in the bulk. Notice that due to the high temperature activation treatment only thermally stable nitrogen substituted for carbon in the ring system can occur (*i.e.* pyrrolic and quaternary nitrogen) [9]. Therefore, the positive effect of nitrogen doping on the thermal stability of UCX can be attributed to the presence of some carbon-nitrogen bonds (615 kJ·mol^{-1}) which are stronger than carbon-carbon bonds (602 kJ·mol^{-1}).

Similar behaviour was observed by Stohr et al., which reported that compared to non-doped carbon materials, nitrogen-doped carbon materials showed higher resistance to oxidation [27].

Overall, Air-TGA results here presented are in agreement with the surface areas previously discussed. Notice that the fact that both ACX$_{5h}$ and UCX present a more ordered structure than CX is also reflected in their lower surface areas (*i.e.* 960 m^2·g^{-1} and 550 m^2·g^{-1} vs 1050 m^2·g^{-1}).

4.1.4 Scanning Electron Microscopy

SEM images of all carbon xerogels are shown in Figure 4. As reported in the literature, carbon xerogels are composed of interconnected and semi-spherical particles, which form a three-dimensional network [9,57]. The fact that all the supports shown in the SEM images presented a relatively similar surface morphology, suggests that both carbon dioxide activation treatment and the doping with nitrogen did not significantly change the surface of the carbon xerogel.

4.2 Characterization of ruthenium-based catalysts supported on carbon xerogels
4.2.1 Transmission Electron Microscopy

Ruthenium particle size distributions of un-promoted and sodium-promoted catalysts are shown in Figure 5 and Figure 6, respectively. It is widely accepted that oxygen surface groups can behave as anchoring sites for metal atoms, improving their dispersion throughout the support [13,15,49]. However, as can be seen in Table 4, despite Ru-CX presented the highest amount of oxygen surface groups, it had the largest average particle size and the lowest metal particles dispersion (*i.e.* 2.4 nm and 30%, respectively) compared to the other un-promoted catalysts herein presented. Similar behaviour was observed by Van Dam et al. [13], which concluded that acidic electron-withdrawing oxygen surface groups (*i.e.* carboxylic, anhydride, lactone) can weaken the interaction between the metal atoms and the support, facilitating their mobility and agglomeration into larger particles. This agrees with the fact that catalysts with the lowest average particle size and highest metal dispersion, Ru-ACX$_{5h}$ and Ru-UCX, also showed the lowest amount of lactone groups.

Similar trend was observed for sodium-promoted catalysts; the lower the amount of lactone groups, the smaller ruthenium average particle size. However, notice that the ruthenium average particle size of sodium-promoted catalysts was larger than that of un-promoted ones (*i.e.* 2.6 - 3.0 nm vs 1.9 - 2.4 nm). Despite the low contrast between ruthenium and sodium, which make very difficult to distinguish ruthenium particles from sodium ones, this behaviour tentatively suggests that metal particles observed Figure 6 are a mixture of ruthenium and sodium atoms.

As depicted in Figure 5, the ruthenium particle size distribution of un-promoted catalysts shifted to the right after the first reaction run. The increase in the average size of ruthenium particles (*i.e.* from 1.9 - 2.4 nm to 2.4 - 2.8 nm) can be explained by the sintering of ruthenium particles due to the high reaction temperature (*i.e.* 600°C). This behaviour was also reported by García-García et al., who pointed out the effect of the reduction temperature on the ruthenium particle size [25].

However, as it can be seen in Figure 6, the ruthenium particle size distribution of sodium-promoted catalysts did not change after the first run of reaction. This strongly suggests that sodium oxide must be located around ruthenium particles, preventing their sintering and agglomeration. This hypothesis is based on Tennison et al. work, who reported that sodium oxide can be found in three different positions with respect to the ruthenium; i) absorbed in the bulk of the ruthenium particles, ii) around the ruthenium particles forming "hot rings", iii) decorating the surface of ruthenium particles [67]. The role of sodium oxide as structural promoter was also reported by García-García et al., who observed that the reduction temperature did not affect the ruthenium particle size of sodium-promoted catalysts [25].

Overall, the TEM results are in good agreement with what evidenced by the STEM/EDS analysis, that is the absence of ruthenium particles aggregates and the potential presence of sodium oxide surrounding ruthenium particles in the "hot rings" configuration. However, looking at the STEM/EDS images in Figure 7, the exact relative position of sodium particles with respect to ruthenium ones is still debatable.

4.2.2 Temperature Programmed Reduction

As can be seen in Figure 8A, three hydrogen reduction peaks were observed for un-promoted catalysts here studied. The first peak observed at low temperature (*i.e.* peak *a*: 210 - 245°C) corresponds to the reduction of the ruthenium oxide particles. The fact that reduction temperature here reported is higher compared with those reported in the literature (*i.e.* 130 - 180°C) [26,55,68], suggests a stronger metal-support interaction in the catalysts studied in this work. Similar behaviour was reported by Yin et al., who found that the interaction between the metal and the support can significantly influence the reduction temperature [3]. Moreover, as expected, the reduction temperature of ruthenium oxide particles increased with their average particle size.

The second reduction peak observed at intermediate temperature (*i.e.* peak *b*: 335 - 420°C), can be explained due to the hydrogen spillover from ruthenium atoms onto

the carbon surface. According to Psofogiannakis et al., the hydrogen spillover is facilitated when the carbon substrate is decorated with oxygen surface groups [69]. Moreover, Guerrero et al. found out that an increased surface density of carboxylic and lactones groups lead to a significant enhancement of the hydrogen spillover [70]. This is consistent with the fact that among all the catalysts Ru-CX, which had the highest amount of carboxylic and lactones groups among all catalysts studied, displayed the highest intensity hydrogen consumption peak attributed to the hydrogen spillover. Notice that under the ammonia decomposition reaction conditions the hydrogen spillover can occur, resulting in a hydrogen rich surface around the ruthenium particles that can affect the catalytic performance.

The third reduction peak observed at high temperature (*i.e.* peak c: 500 - 600°C) corresponds to the partial gasification of the carbon support to produce methane. The temperature range at which this peak is observed is higher than the values reported in the literature [5,6]. In this respect, it has been reported that the extent of the gasification process is determined by the nature of the carbon support. According to Forni et al. [71] and Kowalczyk et al. [72], the gasification process is less pronounced on more crystalline carbon support structures. This could explain the fact that both carbon dioxide activation treatment and nitrogen doping significantly improved the gasification resistance of Ru-ACX$_{1h}$, Ru-ACX$_{5h}$ and Ru-UCX compared to that of Ru-CX.

Sodium-promoted catalysts TPR profiles are shown in Figure 8B. Unlike un-promoted catalysts, only hydrogen consumption peaks corresponding to the reduction of the ruthenium oxide particles (*i.e.* peak d: 375 - 390°C) and the partial gasification of the support (*i.e.* peak e: 540 - 615°C) were observed. This suggests, in accordance with the STEM/EDS and TEM results discussed before, that sodium oxide act as a barrier around ruthenium particles, which avoids the diffusion of hydrogen atoms from the metal to the support [73]. Hence, the hydrogen consumption peak at intermediate temperature corresponding to hydrogen spillover was not observed in any of sodium-promoted catalysts here studied. Moreover, the addition of sodium oxide resulted in an increase in the reduction of the ruthenium oxide particles and the partial gasification of the support temperatures. Likewise, it is important to highlight that the addition of sodium oxide improved the thermal stability of sodium-promoted catalysts, which allows their use in a wider temperature range.

4.2.3 X-ray photoelectron spectroscopy

XPS spectra of the C1s, O1s and N1s regions of un-promoted catalysts are shown in Figure 9A.

The chemical composition of the surface of carbon xerogels here studied is in agreement with the results of previous works [9,17,50–54].

As expected, the treatments used to modify the properties of carbon xerogels affected the nature of the chemical components on their surface.

In this respect, with regards to the XPS spectra of the C1s region, Ru-ACX$_{5h}$ and Ru-UCX presented the two lowest contributions of amorphous carbon (*i.e.* 19% and 18%, respectively), which is indicative of the higher order of their carbonaceous structure compared to the other catalyst supports studied in this work. This is in agreement with the results of the N$_2$ adsorption (BET) and Air-TGA experiments, which provided evidence of the lower surfaces areas and higher burning temperatures, thus higher crystallinity, of both ACX$_{5h}$ and UCX, compared to CX and ACX$_{1h}$. Furthermore, as shown in the deconvolutions of the XPS spectra of C1s and O1s regions, both Ru-ACX$_{5h}$ and Ru-UCX did not present any contribution that could be ascribed to the presence of lactone groups on their surface. These results are in congruence with the TPD profiles shown in Figure 3, and the N$_2$-TGA data reported in Table 3, which suggested a scarce presence of lactone groups on their surfaces.

It is well established that nitrogen doping results in the incorporation of a variety of nitrogen groups in the carbon lattice [9,36,50,52]. In this respect, the XPS spectra of the N1s region proved the presence of pyridinic, pyrrolic, and quaternary nitrogen groups on the surface of Ru-UCX, with a relative contribution of 20%, 45% and 23%, respectively. These results agree with previous studies, which reported that nitrogen-doped carbon xerogels synthesised using urea as nitrogen precursor present higher contributions of pyrrolic and quaternary nitrogen groups than pyridinic nitrogen groups [9,36].

The deconvolutions of the XPS spectra of sodium-promoted catalysts reported in Figure 9B, of the C1s, O1s and N1s regions, exhibited the same trend as their un-promoted counterparts. However, in the C1s and O1s regions, all sodium-promoted catalysts showed an additional contribution corresponding to the presence of carbon-metal bonds and sodium oxide [54], respectively, which was in accordance with the results of the TEM, STEM/EDS and TPR experiments wherein the presence of sodium particles on the catalyst surface was hypothesised.

4.3 Performance of ruthenium-based catalysts supported on carbon xerogels during the ammonia decomposition reaction

The rate of reaction of un-promoted catalysts during the ammonia decomposition reaction is shown in Figure 10A. The hydrogen spillover effect observed on un-promoted ruthenium-based catalysts during TPR experiments could explain, in part, their higher catalytic activity compared with similar catalyst reported in the literature [1,17,26,49], as pointed out in Table 5. It has been reported that the hydrogen spillover can enhance the catalytic activity during the ammonia decomposition reaction, since it affects the number of active sites available for the adsorption of ammonia oncoming molecules. In particular, a large hydrogen spillover effect encourages the migration of hydrogen species over the surface, increasing the number of active sites available for reaction [3,74].

It was observed that the carbon dioxide activation treatment had a positive effect on the performance of both Ru-ACX$_{1h}$ and Ru-ACX$_{5h}$, which showed higher reaction rates than Ru-CX during the ammonia decomposition reaction. This behaviour can be explained due to higher crystallinity of ACX$_{1h}$ and ACX$_{5h}$ compared to CX. The higher activity of Ru-ACX$_{5h}$ compared to both ACX$_{1h}$ and CX can be justified by to the lower amount of oxygen surface presented by ACX$_{5h}$ compared to ACX$_{1h}$ and CX. It has been stated by Aika et al. [15] and Zhong et al. [14] that oxygen surface groups withdraw electrons from ruthenium atoms, to the detriment of the catalytic performance during the ammonia decomposition reaction. Similar behaviour has been reported by Yin et al., which showed that the catalytic performance of ruthenium catalyst is support-dependent, observing that supports with strong basicity, thus with less acidic oxygen functional groups, are beneficial for the ammonia decomposition reaction [4]. Likewise, the nitrogen doping led to a higher reaction rate for Ru-UCX when compared with Ru-CX. Our hypothesis is that the promoting effect of nitrogen atoms overcame the electron-withdrawing effect of the oxygen surface groups, leading to a more basic catalyst support, thus to an improved catalytic activity. In this regards, it has been reported that nitrogen atoms in the carbon lattice enhance the local basicity and electron density of the support, which improve the catalytic activity during the ammonia decomposition reaction [3,17,28].

As shown in Figure 10A, all un-promoted catalysts exhibited higher reaction rates during the second reaction run. This behaviour could be tentatively explained due to the formation of ruthenium B5 sites after the exposure of the catalysts at high temperature (*i.e.* 600°C). It is well established that the ammonia decomposition

reaction is structure sensitive, presenting a reaction rate dependent on the geometry of the metal particles [17,75,76]. Ruthenium B5 sites consist in an ensemble of five edge atoms which encourage the ammonia decomposition reaction by speeding up the nitrogen desorption [75,76]. According to Van Hardeveld and Van Montfoort, the amount B5 sites is maximised when the ruthenium metal particle size is between approximately 2.5 and 5 nm [75]. This is in line with TEM results, which showed that the ruthenium particle after the first reaction run is higher than 2.5 nm in all the catalysts.

The performance of sodium-promoted catalysts during the ammonia decomposition reaction is shown in Figure 11A. The enhanced catalytic activity of sodium-promoted catalysts can be attributed to the electron donor effect of sodium oxide on ruthenium particles. In particular, it was found by Rarog et al., that sodium oxide modified the electrostatic potential around B5 sites, making them more active for the nitrogen dissociation [24].

Moreover, the fact that the catalytic behaviour of sodium-promoted catalysts did not change during the second reaction run suggests that sodium oxide acted as structural promoter, which avoided sintering and agglomeration of ruthenium particles, as also shown by TEM and STEM results previously discussed.

Finally, results shown in Figure 10B, Figure 11B and in Table 6, proved the stability of this catalyst systems under the operating conditions adopted (*i.e.* 450°C, 1 atm). In this regards, after the stability test, all catalysts here studied showed approximately 1.5 wt.% of ruthenium and 5.0 wt.% of sodium with a difference in metal loading within the measurement error (*i.e.* ± 3%), showing a high catalyst-preservability. Key parameters characterising all catalysts here studied, such as i) ruthenium particle size, ii) reaction rate, iii) activation energy, iv) 10% conversion temperature, and v) metal loading, are listed in Table 6.

5 Conclusions

This study has proved that carbon xerogels are efficient catalyst supports for the ammonia decomposition reaction, and that the performance of ruthenium-based catalysts are affected by several factors, including textural and structural properties of the catalyst support, ruthenium particle size distribution and use of sodium as catalyst promoter.

For instance, it has been found that despite the highest hydrogen spillover contribution, Ru-CX exhibited the worst catalytic performance when compared to the other catalysts herein studied. Indeed, both the CO_2 activation treatments at high

temperature and the nitrogen-doping resulted in carbon xerogels with enhanced crystallinity, which can explain the enhanced catalytic performance of Ru-ACX$_{1h}$, Ru-ACX$_{5h}$ and Ru-UCX compared to Ru-CX (*i.e.* 1.9, 3.5 and 3.2 times higher reaction rates, respectively). Furthermore, the improved catalytic performance of both Ru-ACX$_{5h}$ and Ru-UCX can be justified by the higher basicity and electron donor effect of both ACX$_{5h}$ and UCX compared to the other supports.

Likewise, higher reaction rates were observed in catalysts with a ruthenium average particle size higher than 2.5 nm, confirming that the ammonia decomposition reaction is sensitive to the structure, and suggesting the presence of B5 sites in aforementioned catalysts.

Finally, the addition of sodium had a remarkably positive effect on the performance of all catalysts studied during the ammonia decomposition reaction. In this respect, metallic sodium acted as electronic promoter due to its electron donor effect on the ruthenium particles, whereas sodium oxide acted as structural promoter, preventing the sintering of ruthenium particles during the reaction.

Acknowledgements

References

[1]   S.F. Yin, B.Q. Xu, C.F. Ng, C.T. Au, Appl. Catal. B Environ. 48 (2004) 237–241.

[2]   S.F. Yin, Q.H. Zhang, B.Q. Xu, W.X. Zhu, C.F. Ng, C.T. Au, J. Catal. 224 (2004) 384–396.

[3]   S.F. Yin, B.Q. Xu, W.X. Zhu, C.F. Ng, X.P. Zhou, C.T. Au, in: Catal. Today, 2004, pp. 27–38.

[4]   S.F. Yin, B.Q. Xu, X.P. Zhou, C.T. Au, Appl. Catal. A Gen. 277 (2004) 1–9.

[5]   J. Zhang, H. Xu, Q. Ge, W. Li, Catal. Commun. 7 (2006) 148–152.

[6]   M. Melchionna, S. Marchesan, M. Prato, P. Fornasiero, Catal. Sci. Technol. 5 (2015) 3859–3875.

[7]   C. Lin, J.A. Ritter, Carbon N. Y. 38 (2000) 849–861.

[8]   T. Horikawa, J. Hayashi, K. Muroyama, Carbon N. Y. 42 (2004) 1625–1633.

[9]   H.F. Gorgulho, F. Gonçalves, M.F.R. Pereira, J.L. Figueiredo, Carbon N. Y. 47 (2009) 2032–2039.

[10]   M.G. Plaza, F. Rubiera, J.J. Pis, C. Pevida, Appl. Surf. Sci. 256 (2010) 6843–6849.

[11]   T.E. Bell, L. Torrente-Murciano, Top. Catal. 59 (2016) 1438–1457.

[12]   X. Duan, J. Ji, X. Yan, G. Qian, D. Chen, X. Zhou, ChemCatChem 8 (2016) 938–945.

[13]   H.E. Van Dam, H. Van Bekkum, J. Catal. 131 (1991) 335–349.

[14]   Z.H. Zhong, K.I. Aika, J. Catal. 173 (1998) 535–539.

[15]   K. Aika, H. Hori, A. Ozaki, J. Catal. 27 (1972) 424–431.

[16]   W. Raróg, Z. Kowalczyk, J. Sentek, D. Składanowski, D. Szmigiel, J. Zieliñski, Appl. Catal. A Gen. 208 (2001) 213–216.

[17]   F.R. García-García, J. Álvarez-Rodríguez, I. Rodríguez-Ramos, A. Guerrero-Ruiz, Carbon N. Y. 48 (2010) 267–276.

[18]   X. Duan, J. Zhou, G. Qian, P. Li, X. Zhou, D. Chen, Chinese J. Catal. 31 (2010) 979–986.

[19]   R.Z. Sørensen, A. Klerke, U. Quaade, S. Jensen, O. Hansen, C.H. Christensen, Catal. Letters 112 (2006) 77–81.

[20]   K.P. DE JONG, J.W. GEUS, Catal. Rev. 42 (2000) 481–510.

[21]   I. Rossetti, N. Pernicone, L. Forni, Catal. Today 102–103 (2005) 219–224.

[22]   M.C.J. Bradford, P.E. Fanning, M.A. Vannice, J. Catal. 172 (1997) 479–484.

[23]   X. Duan, J. Zhou, G. Qian, P. Li, X. Zhou, D. Chen, Chinese J. Catal. - CHIN J CATAL 31 (2010) 979–986.

[24]   W. Raróg-pilecka, D. Szmigiel, Z. Kowalczyk, 218 (2003) 465–469.

[25]   F.R. García-García, A. Guerrero-Ruiz, I. Rodríguez-Ramos, in: Top. Catal., 2009, pp. 758–764.

[26]   A.K. Hill, L. Torrente-Murciano, Appl. Catal. B Environ. 172 (2015) 129–135.

[27]   B. Stöhr, H.P. Boehm, R. Schlögl, Carbon N. Y. 29 (1991) 707–720.

[28]   R. Czerw, M. Terrones, J.-C. Charlier, X. Blase, B. Foley, R. Kamalakaran, N. Grobert, H. Terrones, D. Tekleab, P.M. Ajayan, others, Nano Lett. 1 (2001) 457–460.

[29]   W. Shen, Z. Li, Y. Liu, Recent Patents Chem. Eng. 1 (2012) 27–40.

[30]   P. Ayala, R. Arenal, M. Rümmeli, A. Rubio, T. Pichler, Carbon N. Y. 48 (2010) 575–586.

[31]   L.M. Ombaka, P.G. Ndungu, V.O. Nyamori, J. Mater. Sci. 50 (2015) 1187–1200.

[32]   S. Ren, F. Huang, J. Zheng, S. Chen, H. Zhang, Int. J. Hydrogen Energy 42 (2017) 5105–5113.

[33]   S.A. Al-Muhtaseb, J.A. Ritter, Adv. Mater. 15 (2003) 101–114.

[34]   H.T. Gomes, P. V. Samant, P. Serp, P. Kalck, J.L. Figueiredo, J.L. Faria, Appl. Catal. B Environ. 54 (2004) 175–182.

[35]   S. Lambert, N. Job, L. D'Souza, M.F.R. Pereira, R. Pirard, B. Heinrichs, J.L. Figueiredo, J.P. Pirard, J.R. Regalbuto, J. Catal. 261 (2009) 23–33.

[36]   J.P.S. Sousa, M.F.R. Pereira, J.L. Figueiredo, Appl. Catal. B Environ. 125 (2012) 398–408.

[37]   R.P. Rocha, J. Restivo, J.P.S. Sousa, J.J.M. Órfão, M.F.R. Pereira, J.L. Figueiredo, Catal. Today 241 (2015) 73–79.

[38]   R.W. Pekala, J. Mater. Sci. 24 (1989) 3221–3227.

[39]   F.J. Maldonado-Hódar, M.A. Ferro-García, J. Rivera-Utrilla, C. Moreno-Castilla, Carbon N. Y. 37 (1999) 1199–1205.

[40]   N. Job, M.F.R. Pereira, S. Lambert, A. Cabiac, G. Delahay, J.F. Colomer, J. Marien, J.L. Figueiredo, J.P. Pirard, J. Catal. 240 (2006) 160–171.

[41]   B.F. Machado, H.T. Gomes, P. Serp, P. Kalck, J.L. Figueiredo, J.L. Faria, Catal. Today 149 (2010) 358–364.

[42]   M.S. Contreras, C.A. Páez, L. Zubizarreta, A. Léonard, S. Blacher, C.G. Olivera-Fuentes, A. Arenillas, J.-P. Pirard, N. Job, Carbon N. Y. 48 (2010) 3157–3168.

[43]   M.B. Barbosa, J.P. Nascimento, P.B. Martelli, C.A. Furtado, N.D.S. Mohallem, H.F. Gorgulho, Microporous Mesoporous Mater. 162 (2012) 24–30.

[44]   S.A. Messele, O. Soares, J.J.M. Órfão, C. Bengoa, J. Font, Environ. Technol. 39 (2018) 2951–2958.

[45] J.W. Arblaster, Platin. Met. Rev. 57 (2013) 127–136.

[46] K.S.W. Sing, Pure Appl. Chem. 57 (1985) 603–619.

[47] J.L. Figueiredo, J. Mater. Chem. A 1 (2013) 9351–9364.

[48] F.R. García-García, A. Guerrero-Ruiz, I. Rodríguez-Ramos, A. Goguet, S.O. Shekhtman, C. Hardacre, Phys. Chem. Chem. Phys. 13 (2011) 12892–12899.

[49] F.R. García-García, E. Gallegos-Suarez, M. Fernández-García, A. Guerrero-Ruiz, I. Rodríguez-Ramos, Appl. Catal. A Gen. 544 (2017) 66–76.

[50] K.Y. Kang, B.I. Lee, J.S. Lee, Carbon N. Y. 47 (2009) 1171–1180.

[51] A.K. Bhattacharya, D.R. Pyke, R. Reynolds, G.S. Walker, C.R. Werrett, J. Mater. Sci. Lett. 16 (1997) 1–3.

[52] K. Jurewicz, K. Babeł, A. Źiółkowski, H. Wachowska, Electrochim. Acta 48 (2003) 1491–1498.

[53] D.J. Morgan, Surf. Interface Anal. 47 (2015) 1072–1079.

[54] V. Dimitrov, T. Komatsu, R. Sato, J. Ceram. Soc. Japan 107 (1999) 21–26.

[55] F.R. García-García, M. Fernández-García, M.A. Newton, I. Rodríguez-Ramos, A. Guerrero-Ruiz, ChemCatChem 5 (2013) 2446–2452.

[56] R.W. Pekala, J.C. Farmer, C.T. Alviso, T.D. Tran, S.T. Mayer, J.M. Miller, B. Dunn, J. Non. Cryst. Solids 225 (1998) 74–80.

[57] L. Zubizarreta, A. Arenillas, J.P. Pirard, J.J. Pis, N. Job, Microporous Mesoporous Mater. 115 (2008) 480–490.

[58] N. Mahata, M.F.R. Pereira, F. Suárez-García, A. Marinez-Alonso, J.M.D. Tascón, J.L. Figueiredo, J. Colloid Interface Sci. 324 (2008) 150–155.

[59] A.M.T. Silva, B.F. Machado, J.L. Figueiredo, J.L. Faria, Carbon N. Y. 47 (2009) 1670–1679.

[60] N. Job, R. Pirard, J. Marien, J.P. Pirard, Carbon N. Y. 42 (2004) 619–628.

[61] R.W. Pekala, F.-M. KONG, Le J. Phys. Colloq. 50 (1989) C4--33.

[62] D. Salinas-Torres, A.F. Léonard, V. Stergiopoulos, Y. Busby, J.J. Pireaux, N. Job, Microporous Mesoporous Mater. 256 (2018) 190–198.

[63] T. Baird, J.R. Fryer, B. Grant, Carbon N. Y. 12 (1974) 591–602.

[64] M. Canal-Rodríguez, N. Rey-Raap, J.Á. Menéndez, M.A. Montes-Morán, J.L. Figueiredo, M.F.R. Pereira, A. Arenillas, Microporous Mesoporous Mater. (2019) 109811.

[65] J.R. Pels, F. Kapteijn, J.A. Moulijn, Q. Zhu, K.M. Thomas, Carbon N. Y. 33 (1995) 1641–1653.

[66] B. Yang, C. Yu, Q. Yu, X. Zhang, Z. Li, L. Lei, Rsc Adv. 5 (2015) 7182–7191.

[67] S.R. Tennison, in: Fundam. Appl. Catal., J.R. Jenni, Plenum Press, New York, 1991.

[68] K. Aika, K. Shimazaki, Y. Hattori, A. Ohya, S. Ohshima, K. Shirota, A. Ozaki, J. Catal. 92 (1985) 296–304.

[69] G.M. Psofogiannakis, G.E. Froudakis, J. Am. Chem. Soc. 131 (2009) 15133–15135.

[70] P. Badenes, L. Daza, I. Rodriguez-Ramos, A. Guerrero-Ruiz, in: Stud. Surf. Sci. Catal., Elsevier, 1997, pp. 241–250.

[71] L. Forni, D. Molinari, I. Rossetti, N. Pernicone, Appl. Catal. A Gen. 185 (1999) 269–275.

[72] Z. Kowalczyk, M. Krukowski, W. Raróg-Pilecka, D. Szmigiel, J. Zielinski, Appl. Catal. A Gen. 248 (2003) 67–73.

[73] R. Prins, Chem. Rev. 112 (2012) 2714–2738.

[74] Q. Su, L. Gu, Y. Yao, J. Zhao, W. Ji, W. Ding, C.T. Au, Appl. Catal. B Environ. 201 (2017) 451–460.

[75] R. van Hardeveld, A. van Montfoort, Surf. Sci. 4 (1996) 396–430.

[76] C.J.H. Jacobsen, S. Dahl, P.L. Hansen, E. Törnqvist, L. Jensen, H. Topsøe, D. V Prip, P.B. Møenshaug, I. Chorkendorff, J. Mol. Catal. A Chem. 163 (2000) 19–26.

Tables

Table 1. Textural and structural properties of carbon xerogels here studied.

Support	S_{BET} (m^2·g^{-1})	Pore volume (cm^3·g^{-1})		
		Total	*Micro*	*Meso*
CX	$1050 \pm 1\%$	$0.39 \pm 1\%$	$0.20 \pm 1\%$	$0.19 \pm 1\%$
ACX$_{1h}$	$1385 \pm 1\%$	$0.41 \pm 1\%$	$0.23 \pm 1\%$	$0.17 \pm 1\%$
ACX$_{5h}$	$960 \pm 1\%$	$0.28 \pm 1\%$	$0.17 \pm 1\%$	$0.11 \pm 1\%$
UCX	$550 \pm 1\%$	$0.24 \pm 1\%$	$0.11 \pm 1\%$	$0.13 \pm 1\%$

Table 2. Comparison between carbon xerogels here studied and those reported in the literature.

Support	R/F	R/C	pH	Carbonisation & Activation	S_{BET} ($m^2 \cdot g^{-1}$)	Ref.
CX	0.50	200	7.11	800 °C / 1 h / N_2	950	This work
CX	0.50	1000	-	900 °C /3.25 h /N_2	630	[42]
CX650	0.50	-	-	650 °C / Ar	663	[50]
CX850	0.50	-	-	850 °C / Ar	771	[50]
CX-750	0.50	-	5.80	750 °C / N_2	644	[64]
C-xerogel	0.50	-	6.40	800 °C / N_2	565-635	[60]
C-xerogel	0.50	-	-	600-1100 °C / N_2	600	[56]
CX-Original	0.50	-	6.00	800 °C / 2 h / N_2	650	[59]
CX-300	0.50	300	6.80	800 °C / N_2	636	[57]
CX-500	0.50	500	6.40	800 °C / N_2	571	[57]
CX-1000	0.50	1000	5.50	800 °C / N_2	657	[57]
13CX-UA	1.85	-	6.00	800 °C / N_2	687	[58]
28CX-UA	1.85	-	5.50	800 °C / N_2	684	[58]
XP350	0.50	350		800 °C / 5 h / N_2	655	[43]
ACX$_{1h}$	0.50	200	7.11	i) 800 °C / 1 h / N_2 ii) 800 °C / 1 h / CO_2	1384	This work
ACX5$_h$	0.50	200	7.11	i) 800 °C / 1 h / N_2 ii) 800 °C / 5 h / CO_2	958	This work
AX-1000	0.50	-	5.80	i) 750 °C / 1 h / N_2 ii) 1000 °C / 2 h / CO_2	1460	[64]
AC-xerogel	1.50	-	-	i) 600-1100 °C / 1 h / N_2 ii) 1050 °C / 3 h / CO_2	600	[56]
CX-800-4	2.50	1000	-	i) 900 °C / 3.25 h / N_2 ii) 800 °C / 4 h / CO_2	670	[42]
UCX	0.50	200	6.02	800 °C / 5 h / N_2	550	This work
URF170	0.50	170	-	800 °C / 5 h / N_2	604	[9]
CXU_5.3_700	0.50	-	5.30	700 °C / N_2	435	[36]
CXU_6.0_700	0.50	-	6.00	700 °C / N_2	432	[36]
CXU_6.9_700	0.50	-	6.90	700 °C / N_2	461	[36]
CXU-6.9	0.50	-	6.90	450 °C / N_2	406	[44]
XU200	0.50	200	-	800 °C / 5 h / N_2	258	[43]

Table 3. Burning temperature (T_{Burn}) and amount (wt.%) of oxygen surface groups of carbon xerogels here studied.

Support	T_{Burn} (°C)	Oxygen surface groups (wt.%)			
		Total	Carboxylic	Anhydrides	Lactones
CX	$535 \pm 0.5\%$	$14.0 \pm 1\%$	$3.5 \pm 1\%$	$4.3 \pm 1\%$	$6.2 \pm 1\%$
ACX$_{1h}$	$580 \pm 0.5\%$	$9.2 \pm 1\%$	$2.1 \pm 1\%$	$2.7 \pm 1\%$	$4.4 \pm 1\%$
ACX$_{5h}$	$600 \pm 0.5\%$	$2.9 \pm 1\%$	$2.0 \pm 1\%$	$0.7 \pm 1\%$	$0.2 \pm 1\%$
UCX	$640 \pm 0.5\%$	$4.6 \pm 1\%$	$3.2 \pm 1\%$	$0.9 \pm 1\%$	$0.5 \pm 1\%$

Table 4. Ruthenium-based catalysts here studied: ruthenium average particle size (*Dp*), SD of ruthenium particle size distributions, and metal particles dispersion (*D(%)*).

Catalyst	Dp (nm)		SD (nm)		D (%)	
	1st	*2nd*	*1st*	*2nd*	*1st*	*2nd*
Ru-CX	2.4	2.8	0.93	1.06	29.9	26.9
Ru/Na-CX	3.0	3.0	0.89	0.93	27	-
Ru-ACX$_{1h}$	2.2	2.6	0.82	0.63	33.7	29.3
Ru/Na-ACX$_{1h}$	2.8	2.8	0.89	0.80	27.6	-
Ru-ACX$_{5h}$	2.0	2.4	0.56	0.78	35.1	32.1
Ru/Na-ACX$_{5h}$	2.6	2.6	0.50	0.71	29.4	-
Ru-UCX	1.9	2.5	0.80	1.05	34.9	32.6
Ru/Na-UCX	2.5	2.6	0.69	0.84	29.9	-

Table 5. Comparison between the performances of the Ru-based catalysts studied in this work (T.W.) and those of the literature during the ammonia decomposition reaction.

Catalyst	Ru (wt. %)	GHSV (ml$_{NH3}$·g$_{cat}^{-1}$·h^{-1})	Operating conditions	TOF (mol$_{NH3}$·mol$_{Ru}^{-1}$·h^{-1})	Ref.
Ru-CX	1.5	2000	1 atm, 350°C	65	T.W.
Ru-ACX$_{1h}$	1.5	2000	1 atm, 350°C	103	T.W.
Ru-ACX$_{5h}$	1.5	2000	1 atm, 350°C	190	T.W.
Ru-UCX	1.5	2000	1 atm, 350°C	163	T.W.
Ru/Na-CX	1.5	2000	1 atm, 350°C	169	T.W.
Ru/Na-ACX$_{1h}$	1.5	2000	1 atm, 350°C	185	T.W.
Ru/Na-ACX$_{5h}$	1.5	2000	1 atm, 350°C	326	T.W.
Ru/Na-UCX	1.5	2000	1 atm, 350°C	236	T.W.
Ru/AC	5.0	6000	1 atm, 400°C	19	[1]
Ru/CNT	5.0	6000	1 atm, 400°C	45	[1]
Ru/AC0	2.0	2000	1 atm, 400°C	75	[49]
Ru/AC1	2.0	2000	1 atm, 400°C	75	[49]
RuCNTs-0	2.0	2000	1 atm, 350°C	13	[17]
RuCNTs-N	2.0	2000	1 atm, 350°C	17	[17]
RuCNTs-1	2.0	2000	1 atm, 350°C	25	[17]
RuCNTs-2	2.0	2000	1 atm, 350°C	128	[17]
Ru/CNT	7.0	5200	1 atm, 327°C	11	[26]
Ru/GCNT	7.0	5200	1 atm, 327°C	77	[26]

Table 6. Ruthenium-based catalysts here studied: rate of reaction at 450°C (*i.e. r_{NH3}*), activation energy (*i.e.* E_a), 10% conversion temperature (*i.e.* T_{10}) before and after the first reaction run, and metal loading after the long-term stability test.

Catalyst	$r_{NH3,450°C}$ (mol·m^{-3}·h^{-1})		E_a (kJ·mol^{-1})		T_{10} (°C)		Metal (wt.%)	
	1st	*2nd*	*1st*	*2nd*	*1st*	*2nd*	*Ru*	*Na*
Ru-CX	5.2X10^3	2.0X10^4	102.6	81.2	380	355	1.35	-
Ru/Na-CX	5.0X10^4	-	82.3	-	340	-	1.32	5.31
Ru-ACX$_{1h}$	9.8X10^3	2.2X10^4	93.3	80.0	360	345	1.37	-
Ru/Na-ACX$_{1h}$	5.3X10^4	-	81.9	-	330	-	1.36	5.35
Ru-ACX$_{5h}$	1.8X10^4	5.3X10^4	88.2	76.6	360	325	1.38	-
Ru/Na-ACX$_{5h}$	7.8X10^4	-	76.1	-	300	-	1.42	5.38
Ru-UCX	1.6X10^4	3.7X10^4	90.9	80.7	350	325	1.32	-
Ru/Na-UCX	5.9X10^4	-	80.2	-	305	-	1.34	5.33

Figures
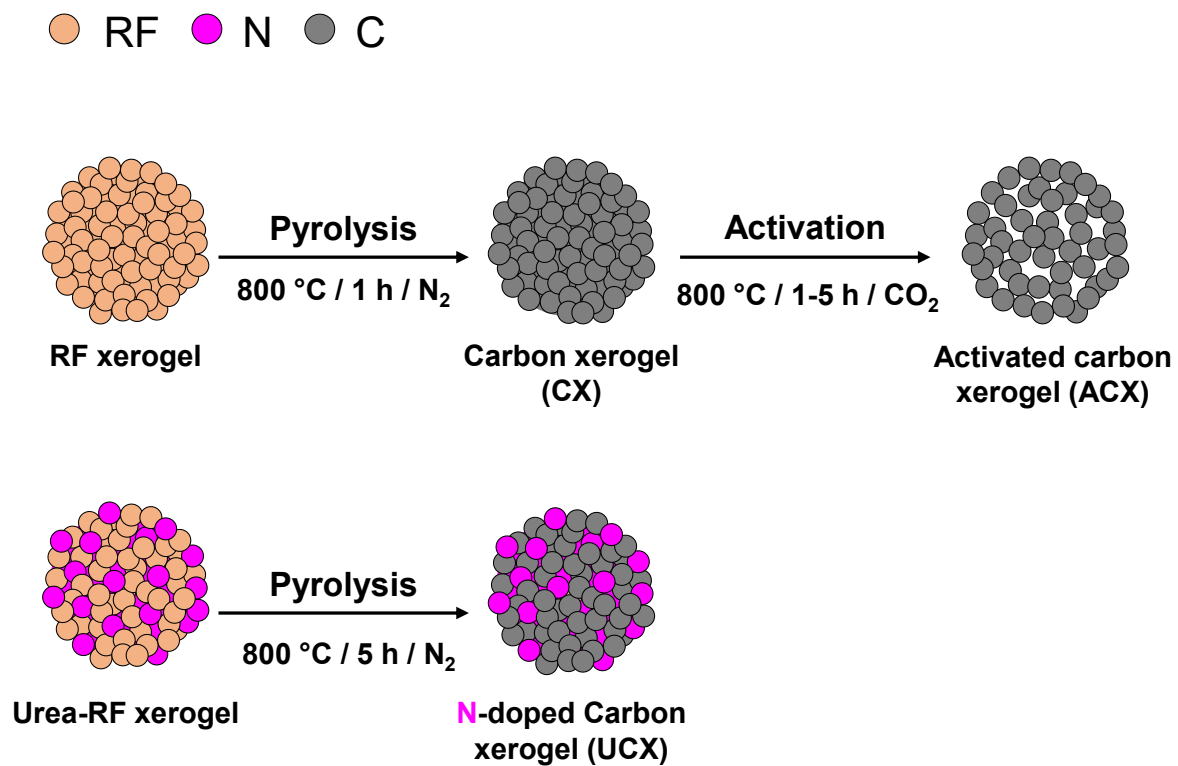
Figure 1. Schematic of the treatments used to synthesise the different carbon xerogels here studied.
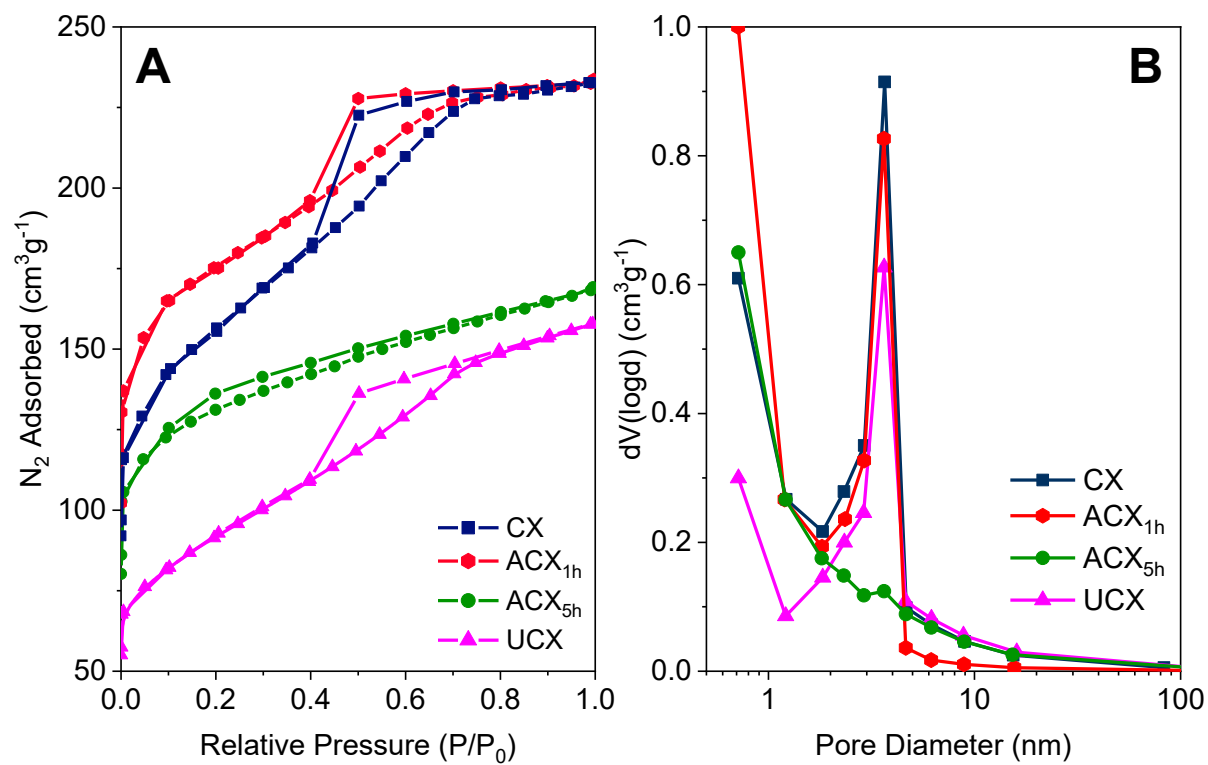
Figure 2. (A) Nitrogen adsorption/desorption isotherms at -196 °C and (B) pore size distributions of carbon xerogels here studied.
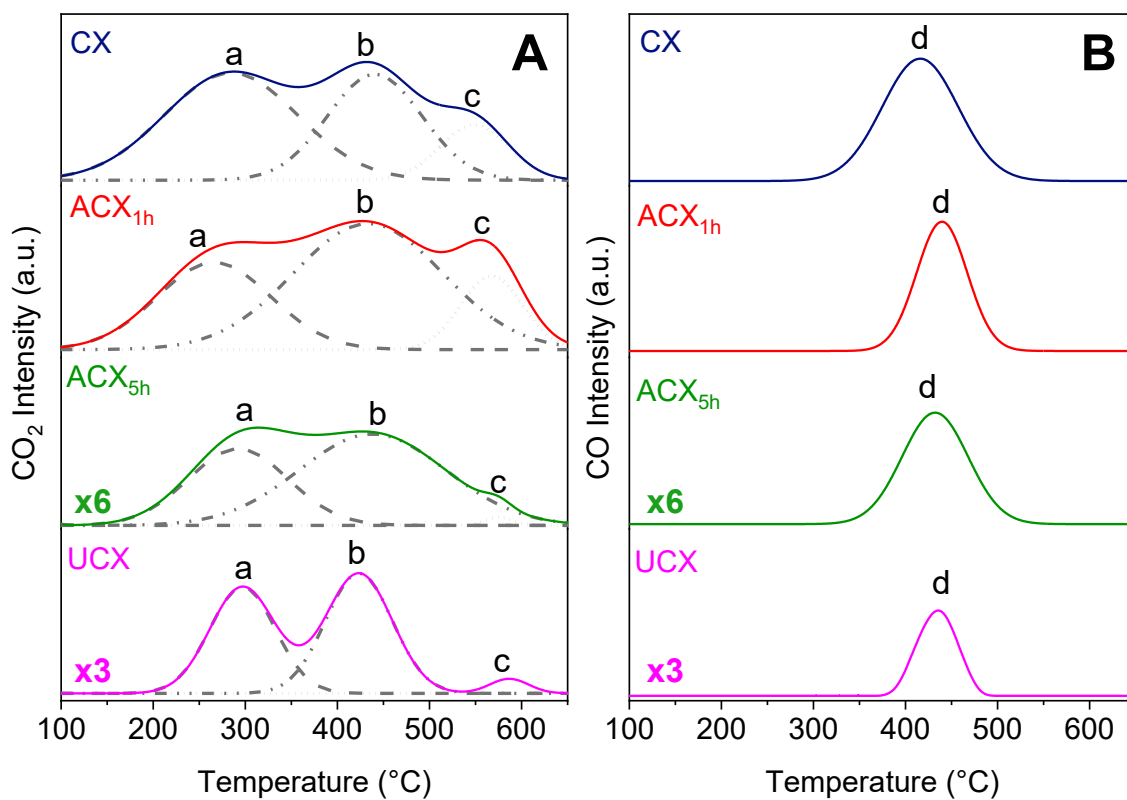
Figure 3. (A) Carbon dioxide and (B) carbon monoxide Temperature Programmed Desorption profiles for carbon xerogels here studied.
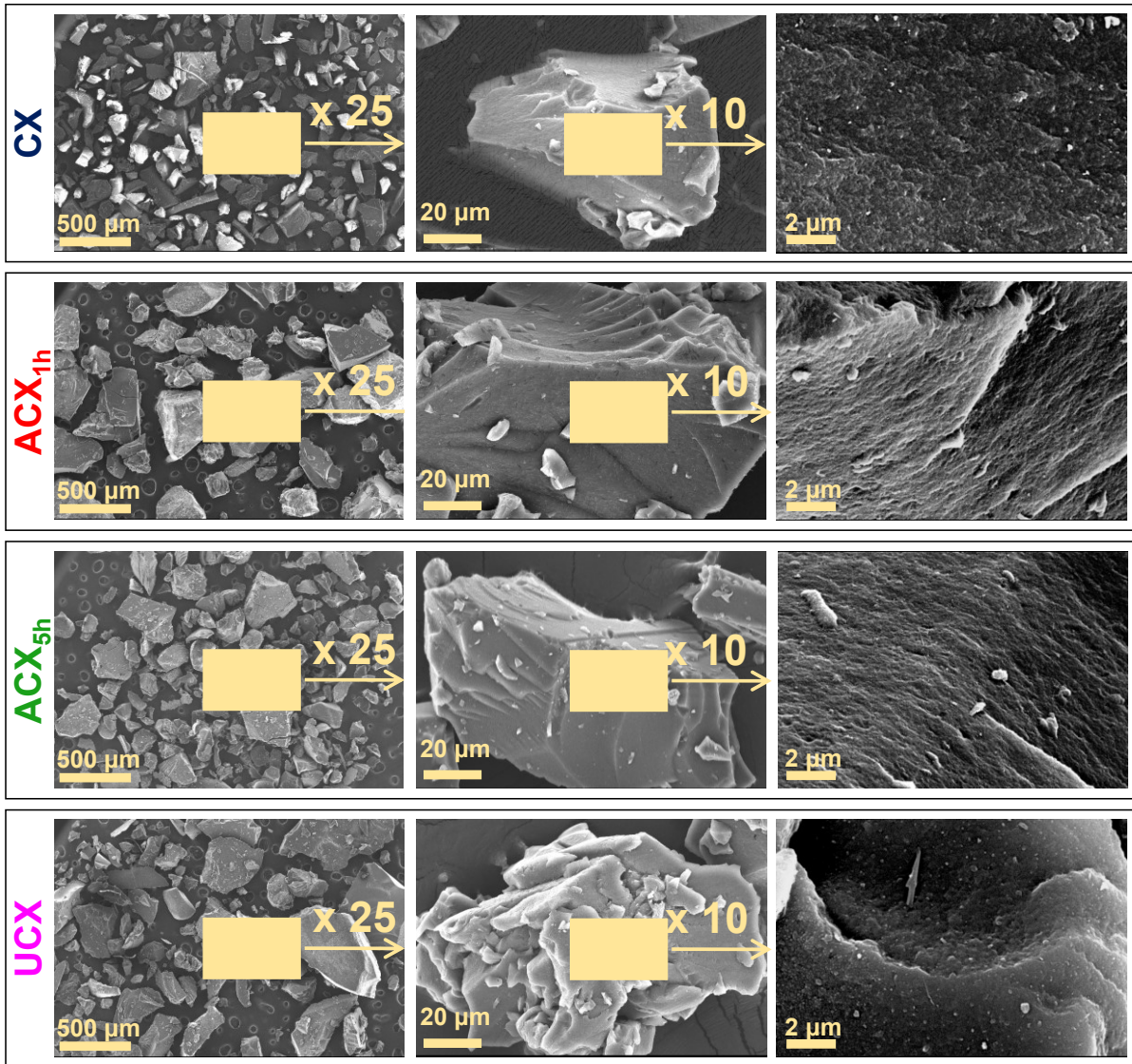
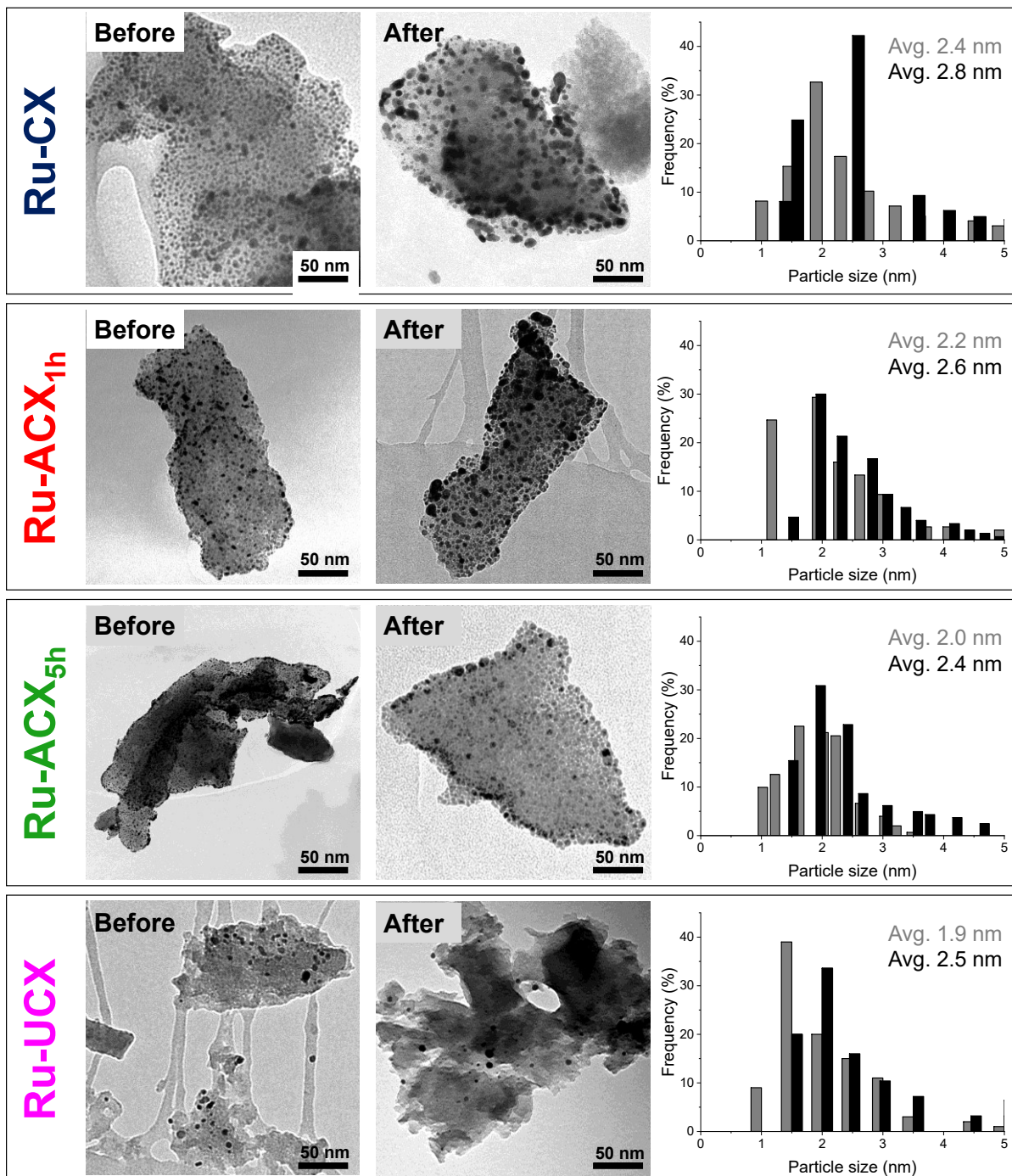Figure 4. SEM images of carbon xerogels at different magnifications.

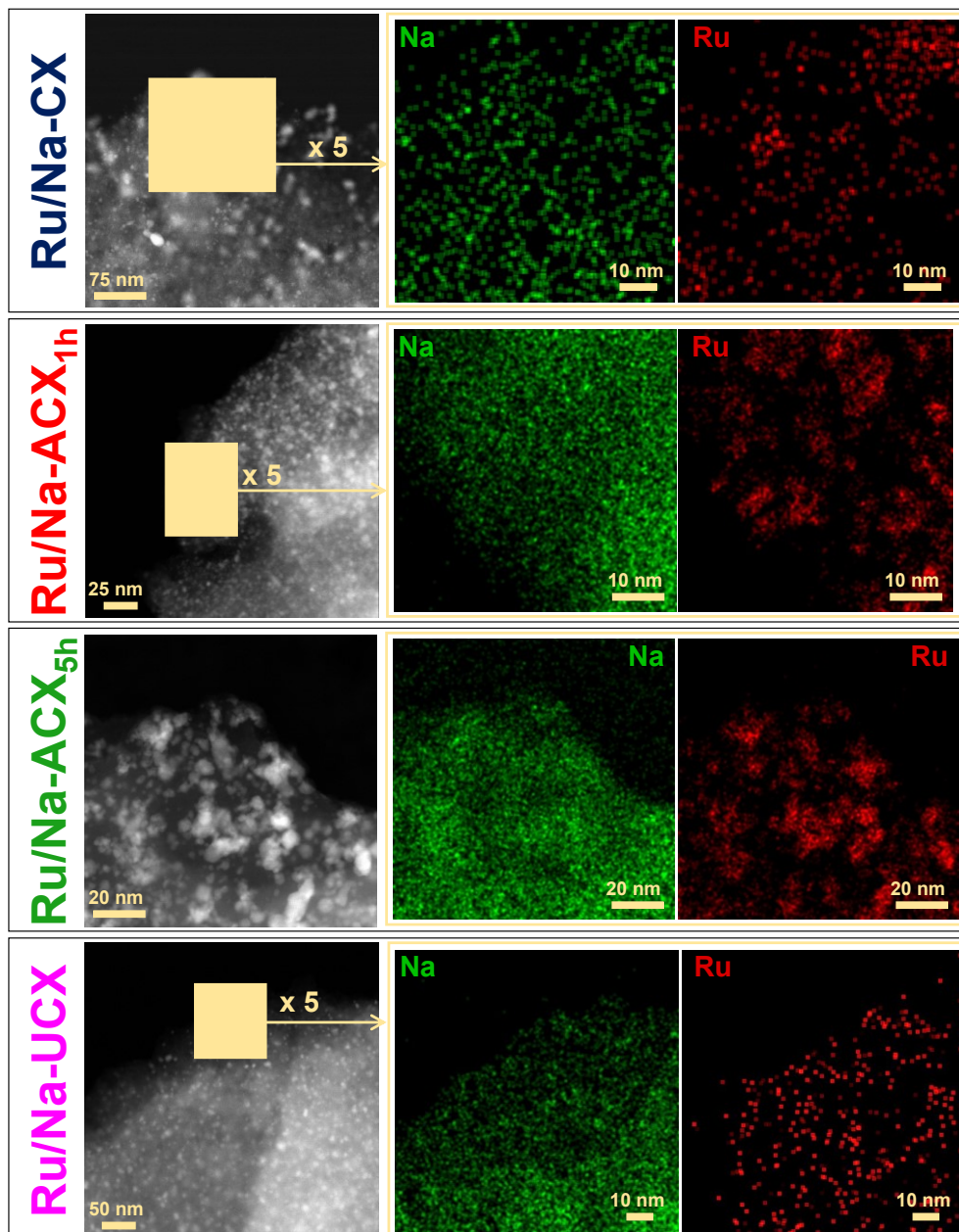Figure 5. TEM images before and after reaction of un-promoted ruthenium-based catalysts. Right: Particle size distributions before (grey) and after (black) reaction.
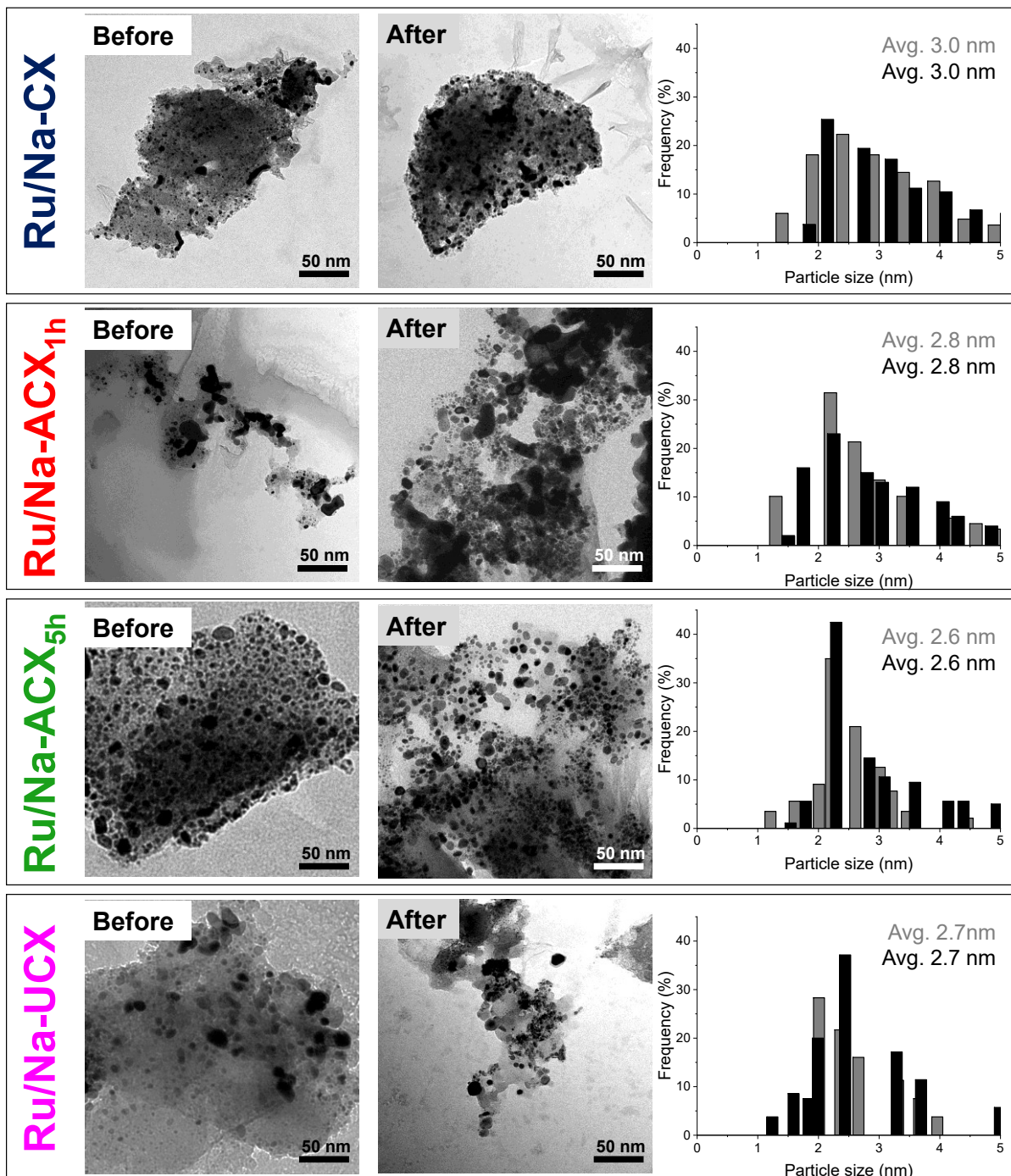
Figure 6. TEM images before and after reaction of sodium-promoted ruthenium-based catalysts. Right: Particle size distributions before (grey) and after (black) reaction.

Figure 7. Representative STEM-HAADF images and corresponding EDS elemental maps taken from the sodium-promoted ruthenium-based catalysts after reaction.
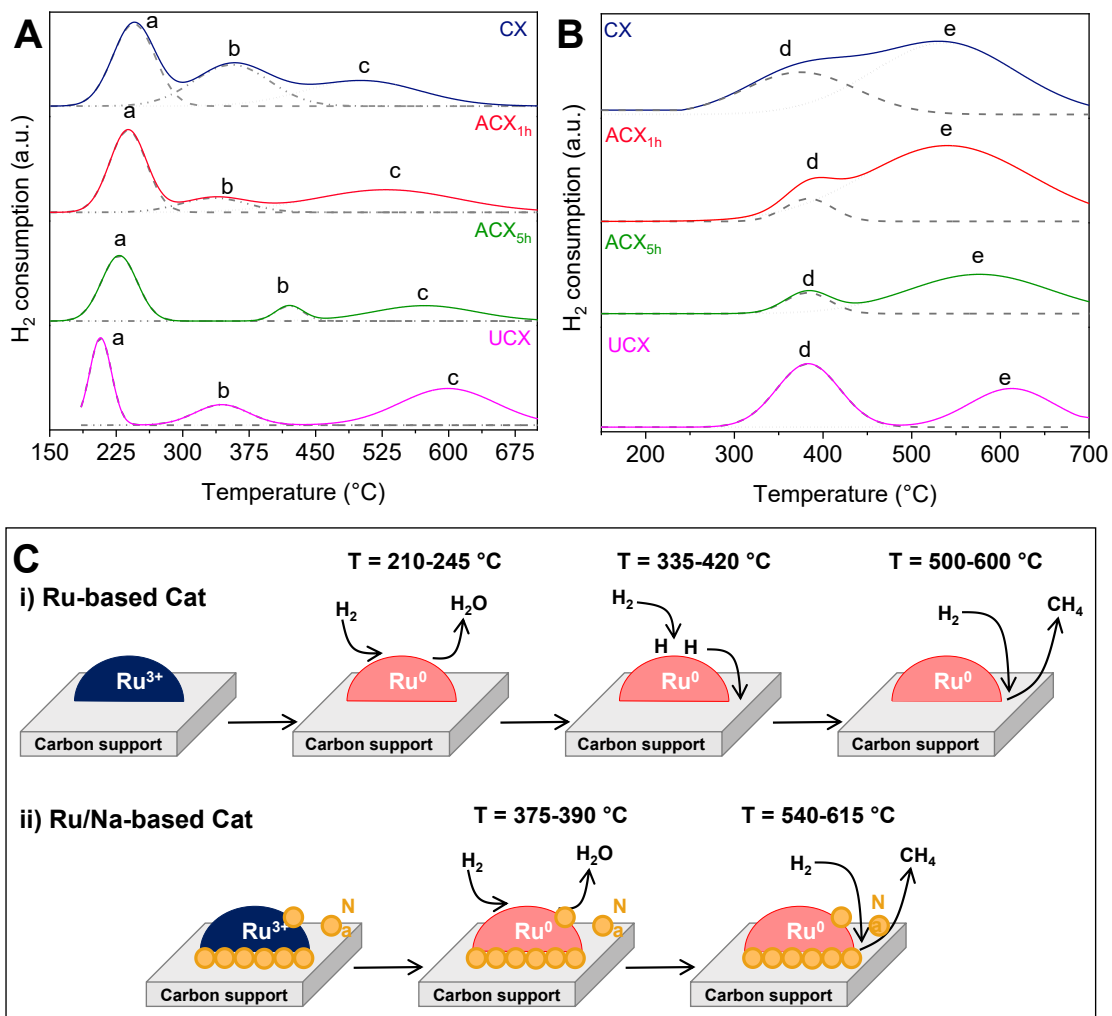
Figure 8. Temperature Programmed Reduction profiles of (A) un-promoted and (B) sodium-promoted ruthenium-based catalyst, and (C) schematic representation of the evolution of the catalysts surface during TPR experiments of un-promoted (i) and sodium-promoted (ii) ruthenium-based catalysts.
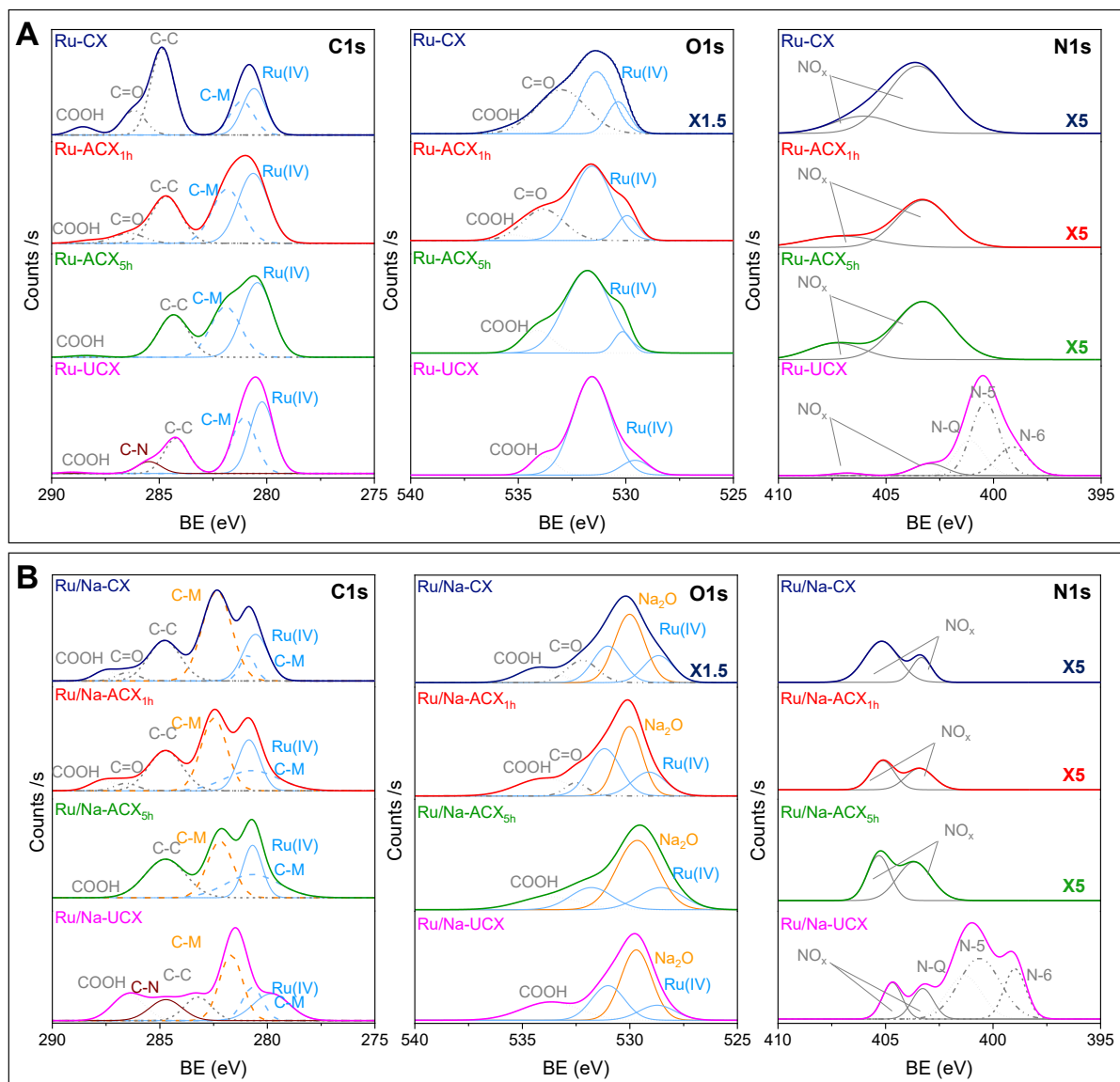
Figure 9. XPS spectra of C1s, O1s and N1s regions for the (A) un-promoted and (B) sodium-promoted ruthenium-based catalysts here studied.
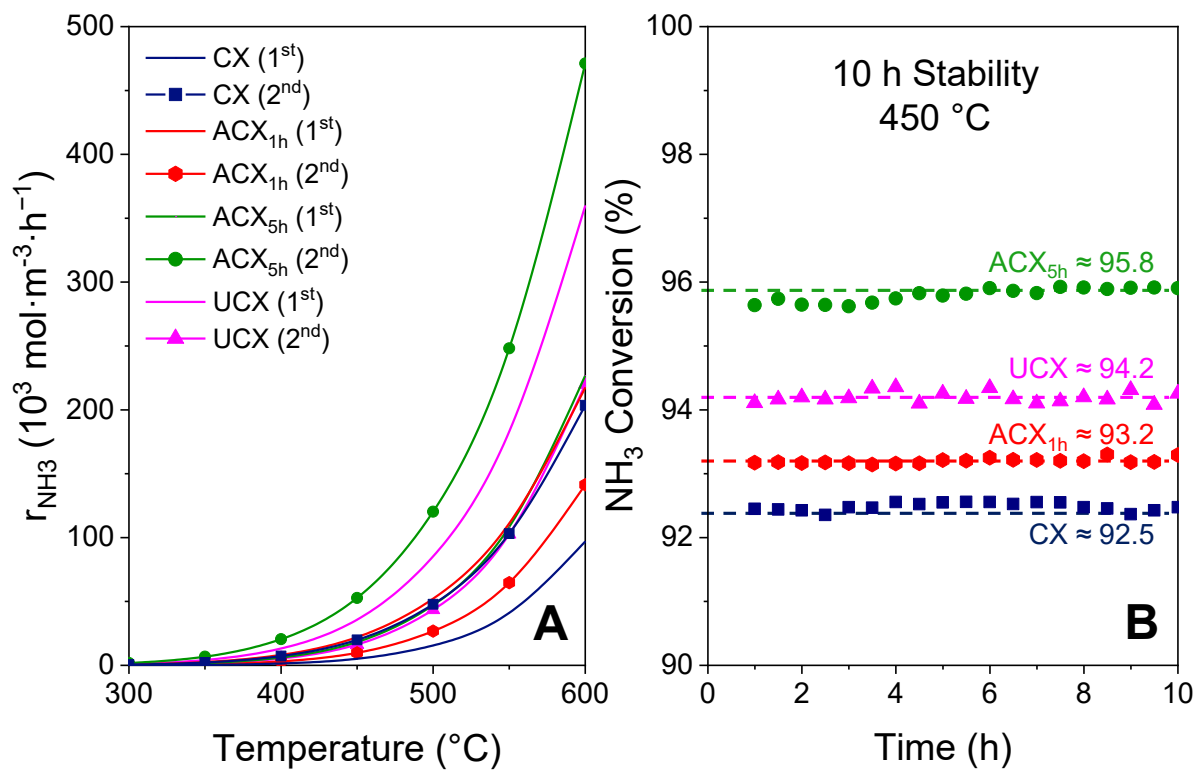
Figure 10. Un-promoted catalysts: (A) Ammonia decomposition reaction rates (B) long-term stability test at 450 °C.
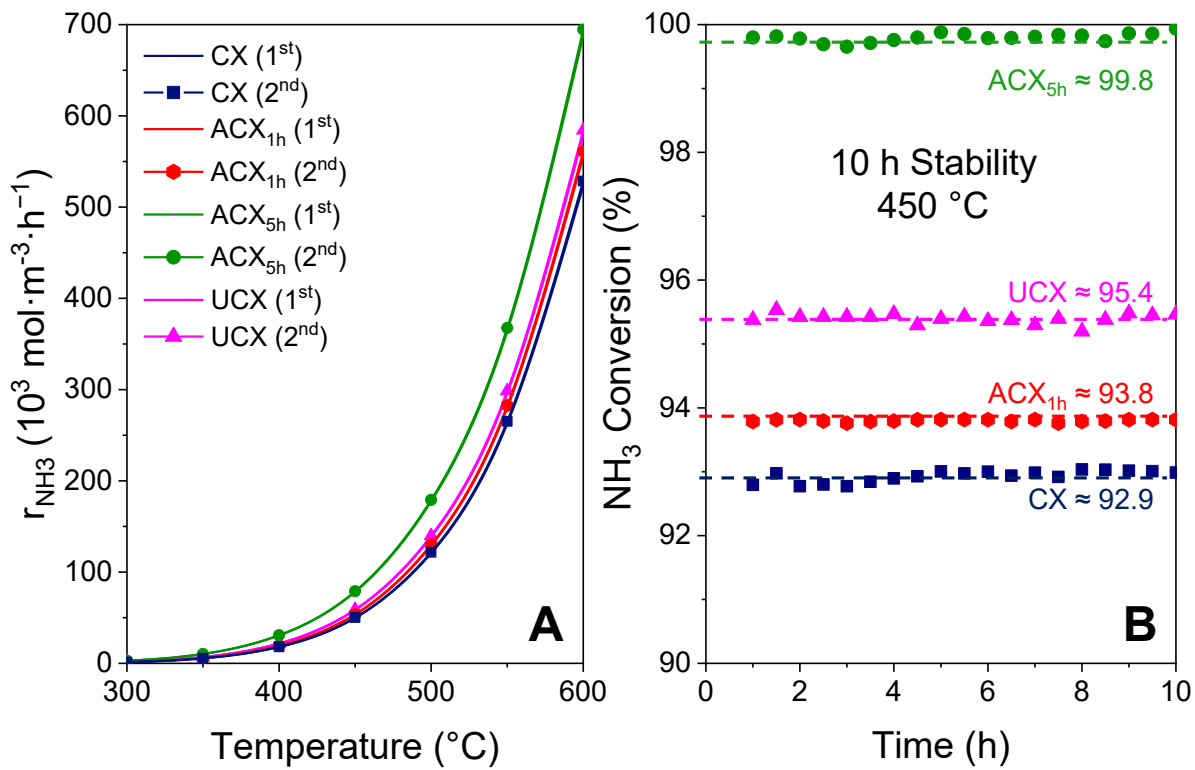
Figure 11. Sodium-promoted catalysts: (A) Ammonia decomposition reaction rates (B) long-term stability test at 450 °C.